

# Materials for multifunctional balloon catheters with capabilities in cardiac electrophysiological mapping and ablation therapy

Dae-Hyeong Kim<sup>1†</sup>, Nanshu Lu<sup>1†</sup>, Roozbeh Ghaffari<sup>2†</sup>, Yun-Soung Kim<sup>1</sup>, Stephen P. Lee<sup>2</sup>, Lizhi Xu<sup>1</sup>, Jian Wu<sup>3</sup>, Rak-Hwan Kim<sup>1</sup>, Jizhou Song<sup>4</sup>, Zhuangjian Liu<sup>5</sup>, Jonathan Viveni<sup>6</sup>, Bassel de Graff<sup>2</sup>, Brian Elolampi<sup>2</sup>, Moussa Mansour<sup>7</sup>, Marvin J. Slepian<sup>8</sup>, Sukwon Hwang<sup>1</sup>, Joshua D. Moss<sup>9</sup>, Sang-Min Won<sup>1</sup>, Younggang Huang<sup>3</sup>, Brian Litt<sup>6,10</sup> and John A. Rogers<sup>1\*</sup>

**Developing advanced surgical tools for minimally invasive procedures represents an activity of central importance to improving human health. A key challenge is in establishing biocompatible interfaces between the classes of semiconductor device and sensor technologies that might be most useful in this context and the soft, curvilinear surfaces of the body. This paper describes a solution based on materials that integrate directly with the thin elastic membranes of otherwise conventional balloon catheters, to provide diverse, multimodal functionality suitable for clinical use. As examples, we present sensors for measuring temperature, flow, tactile, optical and electrophysiological data, together with radiofrequency electrodes for controlled, local ablation of tissue. Use of such 'instrumented' balloon catheters in live animal models illustrates their operation, as well as their specific utility in cardiac ablation therapy. The same concepts can be applied to other substrates of interest, such as surgical gloves.**

Inflatable balloon catheters constitute an extremely simple, yet powerful, class of medical instrument that can deliver therapy or facilitate diagnosis of biological tissues and intraluminal surfaces through direct, soft mechanical contact. In peripheral or coronary angioplasty, inflation of such a device in a stenotic blood vessel can eliminate blockage and, at the same time, effect the expansion of a stent to maintain an open configuration<sup>1,2</sup>. In a different procedure, known as septostomy, the balloon plays a related but more forceful role, as an instrument that creates large passages between the right and left atria, to enable shunting for increased blood flow<sup>3,4</sup>. The balloon-catheter device is attractive for these and other procedures because (1) it enables minimally invasive insertion into lumens or other organs of the body through small incisions, owing to the miniaturized, cylindrical form of its deflated state, and (2) it can be configured, through controlled inflation, to match requirements on size and shape for its interaction with the tissue, where contact occurs in a soft, conformal manner, capable of accommodating complex, curvilinear and time dynamic surfaces in a completely non-destructive manner. The main disadvantage is that conventional balloons offer minimal utility, owing to their construction from uniform sheets of electronically and optically inactive materials, such as polyurethane or silicone.

In this paper, we exploit the balloon catheter as a platform for heterogeneous collections of high-performance semiconductor devices, sensors, actuators and other components. The result is a new type of surgical tool that can provide versatile modes of operation inclusive of but far beyond the simple mechanical manipulations involved in angioplasty, septostomy and other standard procedures. Here, we focus on implementation in cardiac ablation therapy, with several modes of sensory feedback control, designed for the treatment of various types of sustained arrhythmia of the heart, such as atrial fibrillation<sup>5–7</sup>. Current procedures use closed or open irrigation layouts with single, point-source ablation electrodes that offer limited sensing functionality or array capabilities. The time-intensive nature of surgical work carried out with such devices increases the rate of morbidity, and also demands advanced technical skills from the operator<sup>7</sup>. Emerging cryo-, radiofrequency (RF) and laser balloon catheters and multi-electrode structures simplify mechanical manoeuvring and ablation but they do not provide critical information about lesion depth, contact pressure, blood flow or localized temperature<sup>8–17</sup>. The systems reported here overcome these limitations and eliminate the need for further catheters by providing the ability to sense electrical, tactile, optical, temperature

<sup>1</sup>Department of Materials Science and Engineering, Beckman Institute for Advanced Science and Technology, and Frederick Seitz Materials Research Laboratory, University of Illinois at Urbana-Champaign, Urbana, Illinois 61801, USA, <sup>2</sup>MC10 Inc., 36 Cameron Avenue, Cambridge, Massachusetts 02140, USA, <sup>3</sup>Department of Mechanical Engineering and Department of Civil and Environmental Engineering, Northwestern University, Evanston, Illinois 60208, USA, <sup>4</sup>Department of Mechanical and Aerospace Engineering, University of Miami, Coral Gables, Florida 33146, USA, <sup>5</sup>Institute of High Performance Computing, 1 Fusionopolis Way, #16-16 Connexis, 138632, Singapore, <sup>6</sup>Department of Bioengineering, University of Pennsylvania, Philadelphia, Pennsylvania 19104, USA, <sup>7</sup>Massachusetts General Hospital, Harvard Medical School, Boston, Massachusetts 02114, USA, <sup>8</sup>Sarver Heart Center, University of Arizona, Tucson, Arizona 85724, USA, <sup>9</sup>Department of Cardiology, Hospital of the University of Pennsylvania, 9 Founders Pavilion, 3400 Spruce Street, Philadelphia, Pennsylvania 19104, USA, <sup>10</sup>Department of Neurology, Hospital of the University of Pennsylvania, 3 West Gates, 3400 Spruce Street, Philadelphia, Pennsylvania 19104, USA. †These authors contributed equally to this work. \*e-mail: jrogers@uiuc.edu.

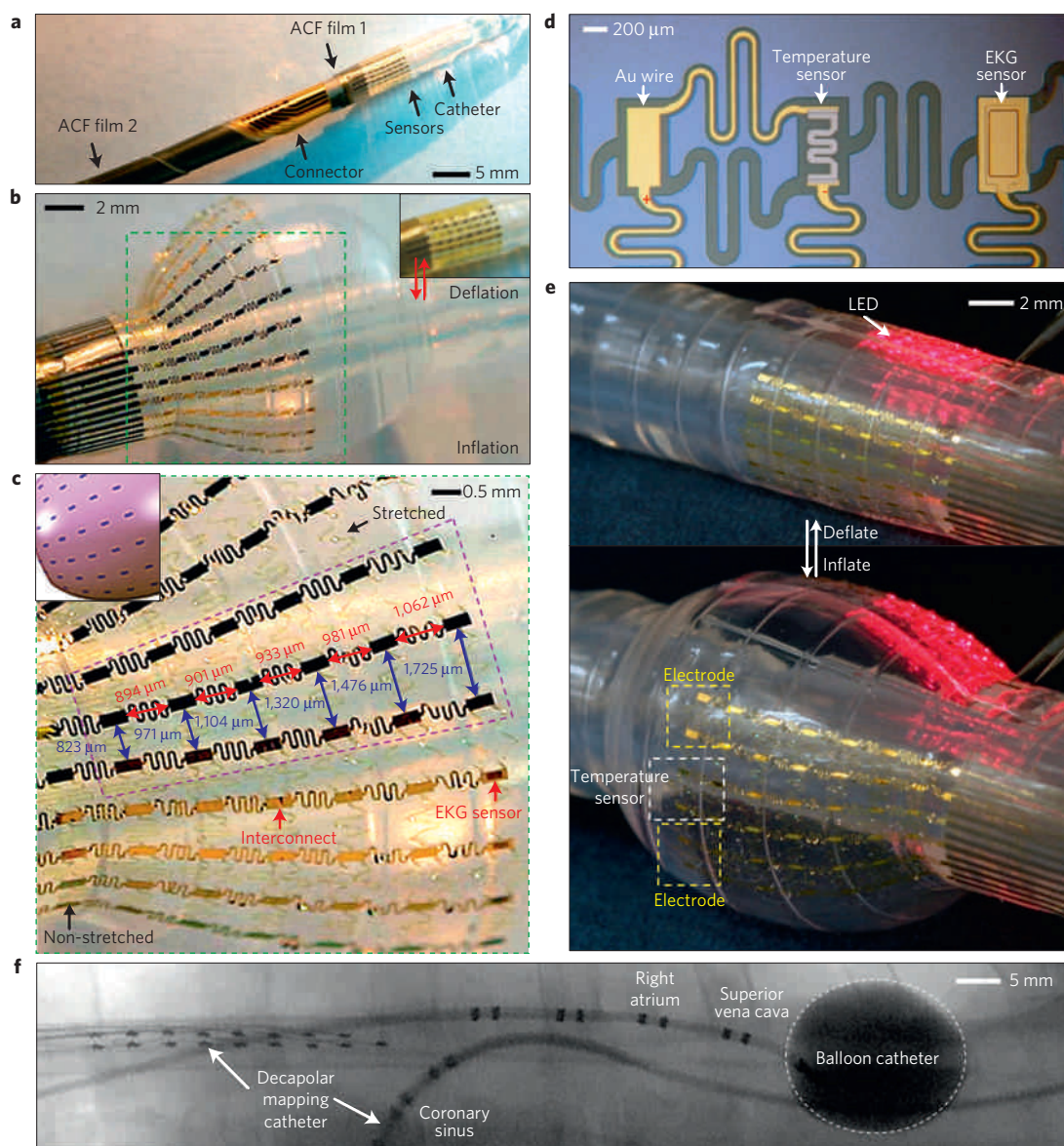


**Figure 1 | Multifunctional inflatable balloon catheters.** **a**, Optical image of a stretchable, interconnected passive network mesh integrated on a balloon catheter (deflated) showing the overall construction, including connectors and ACF metal traces on the proximal side of the balloon and its wrapping configuration along the length of the catheter shaft. **b**, Optical image of the balloon inflated by  $\sim 130\%$  relative to its deflated state (inset). **c**, Magnified view of non-coplanar serpentine interconnects on the balloon in its inflated state. This region corresponds to the area defined by the green dotted line in **b**. The spacings between the islands and the configurations of the serpentine interconnects compare well with simulation results (inset, purple dotted area from Supplementary Fig. S2). **d**, Magnified image of a temperature sensor and gold lines used to apply positive and negative bias voltages. Electrodes for simultaneous electrogram mapping (EKG) are also shown. **e**, Optical image of a multifunctional balloon catheter in deflated and inflated states. The image shows arrays of temperature sensors (anterior), microscale light-emitting diodes (posterior) and tactile sensors (facing downward). **f**, X-ray angiography image of an instrumented balloon catheter deployed in the heart (right atrium) of a pig for *in vivo* recording of electrophysiology near the superior vena cava. The balloon was filled with contrast dye to facilitate imaging.

and flow properties at the tissue–balloon interface, in real time as the procedure is carried out.

Commercially available catheters (8–18 Fr, BARD) serve as platforms for the devices. Components that integrate with the balloons are formed on semiconductor wafers using adapted versions of planar processing techniques and methods of transfer printing reported elsewhere<sup>18</sup>. Wrapping the resulting collections of interconnected devices on the balloon in its deflated state completes the process<sup>19</sup>. Encapsulating layers serve as moisture barriers to enable the entire system to operate when completely immersed in bio-fluids. These devices sense physiological signals and stimulate tissue. They are connected and powered through a thin ribbon

cable based on an anisotropic conductive film (ACF) that bonds to the base of the shaft that connects to the balloon, and wraps along the length of the flexible tubing of the catheter. Key steps in the fabrication and assembly appear in the Methods section and in Supplementary Information. These procedures add functionality to balloons without significantly altering their mechanical properties or the levels of expansion that they can accommodate. The mesh layouts can tolerate tensile strains of up to 200% without fracture, owing to optimized configurations guided by quantitative mechanics modelling.

Figure 1a–c provides images of a balloon-catheter device with a passive, uniform network mesh, to illustrate the

overall construction and mechanics. The strain distributions obtained through analytical and computational modelling capture, quantitatively, the nature of these deformations (inset of Fig. 1c and Supplementary Figs S1–S3). Active and/or passive devices integrate at the nodes of the mesh, minimizing their mechanical coupling to the strains associated with inflation/deflation of the balloon. Demands on layouts and interconnections for functional systems force local modifications of the simple serpentine geometry of Fig. 1a–c (Supplementary Figs S4–S5), as illustrated in Fig. 1d. This micrograph corresponds to part of a multifunctional balloon catheter that supports a temperature sensor and an exposed sensing electrode pad. Active semiconductor devices can also be incorporated. Figure 1e shows a completed system, with microscale light-emitting diodes<sup>20</sup>, sensor electrodes, temperature detectors and other components. After multiple inflation and deflation cycles exceeding 100% strain levels<sup>18,20</sup>, all devices and interconnects undergo little or no performance degradation. Figure 1f presents an X-ray micrograph of a related device, fully deployed in its inflated state within the right atrium. The surface electrodes on the balloon in this case are positioned to record electrical activity near the superior vena cava in a porcine animal model.

We begin by discussing materials and design considerations for various sensors and ablation devices capable of use in cardiac applications. The first is a micro-tactile sensor for detecting dynamic mechanical forces exerted on heart tissue. These devices are important for monitoring mechanical interactions during surgery or diagnosis; they must satisfy, simultaneously, two demanding requirements: (1) minimal sensitivity to in-plane forces, to decouple their operation from inflation/deflation or other deformations of the balloon, and (2) high sensitivity to normal forces, in a soft mechanical construction, to enable non-destructive measurements against low-modulus tissue<sup>21</sup>. Existing sensor technologies are unsuitable for integration on highly stretchable substrates such as balloons<sup>22–26</sup>. More recent tactile sensors based on electrically conducting rubbers or elastomeric dielectrics cannot be used either because responses to in-plane strains conflate with those from normal strains<sup>25,26</sup>.

To address the aforementioned requirements, we exploit two ideas in mechanics. First, as highlighted in Fig. 1, non-coplanar serpentine mesh layouts with devices located at planar nodes experience small strains (<1%), even for large deformations of the substrate<sup>27</sup>. Strains at these locations can be reduced further by decreasing the size of the nodes, and by increasing their thickness and modulus<sup>28</sup>. To exploit these features, we locate our tactile sensors at small nodes on thick (5  $\mu\text{m}$ ) layers of a high-modulus ( $\sim 4$  GPa), photo-definable epoxy (SU8, Microchem). For the second requirement, the stiffness of the sensor in the normal direction must be low and its sensitivity to compression must be high. To this end, we use a pressure-sensitive, electrically conductive silicone rubber (PSR; Elastosil LR 3162, Wacker Silicones) with low stiffness (1.8 MPa), configured in a bridge shape, overlying a rectangular feature of a low-modulus formulation of poly(dimethylsiloxane) (PDMS; 650 kPa). This structure forces current to flow through the narrow, top layer of the PSR bridge. The soft, underlying PDMS imposes little constraint on compression-induced lateral expansion of the PSR, thereby facilitating associated resistance changes. A thin coating of polyimide (PI) cured at 300 °C for an hour encapsulates the entire structure to avoid leakage current. This process does not cause device degradation, thereby suggesting that the system is compatible with temperatures used for sterilization.

Figure 2a presents a cross-sectional schematic drawing of the sensor (left). The in-plane results of finite-element modelling (right panel) illustrate the ability of the epoxy to reduce strains in the PSR induced by expansion of the supporting balloon substrate. The extent of reduction increases with thickness of the epoxy (Supplementary Fig. S6a). Figure 2b presents calculated lateral

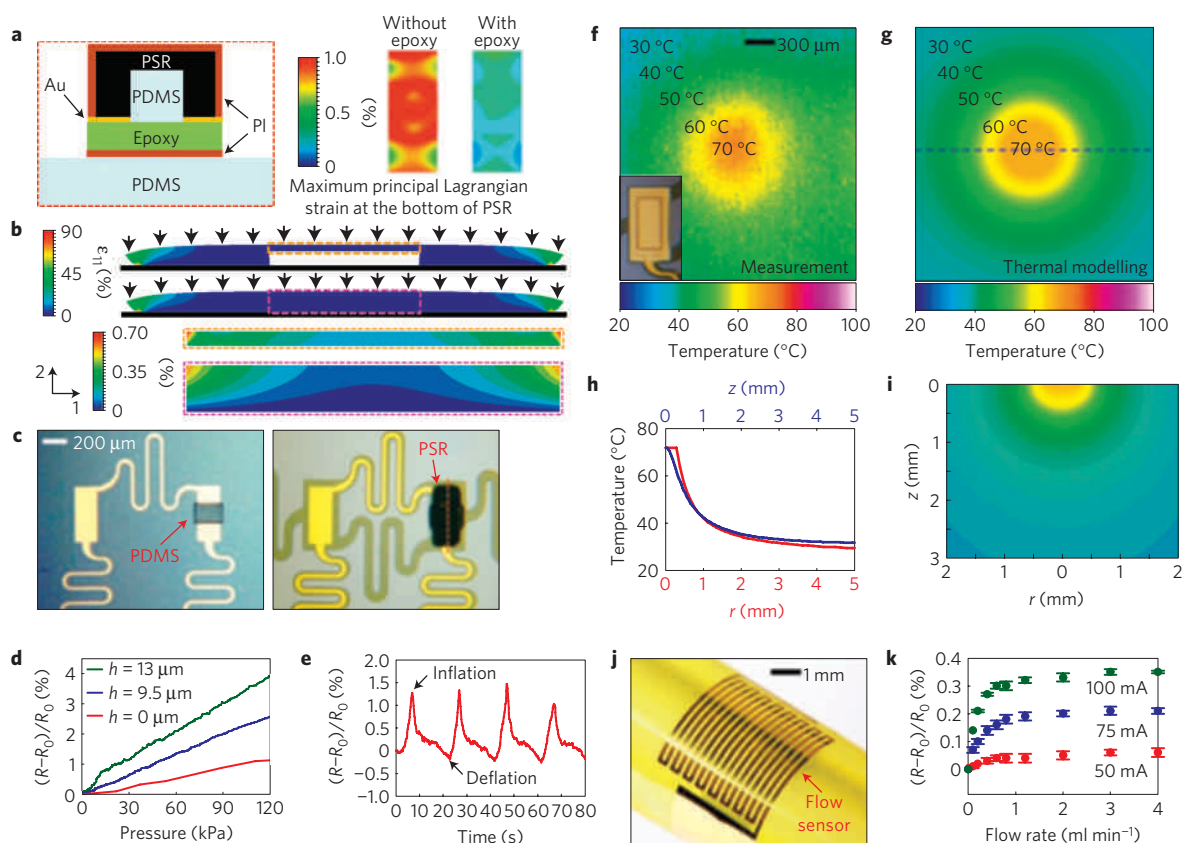
strains in the PSR induced by applying a uniform pressure (1 MPa). With the soft PDMS layer, the bottom of the PSR bridge can expand laterally (orange dotted box). This lateral tensile strain ( $\epsilon_{11}$ ) increases the resistance of the PSR. Without PDMS, the stiff underlying layer of epoxy constrains motion of the PSR, thereby minimizing the lateral expansion strain  $\epsilon_{11}$  near the interface (pink dotted box).

Figure 2c shows optical micrographs at two stages of the process for fabricating sensors with these designs. For details, see the Methods and Supplementary Information. To test these structures, we used a custom-made micro-compression stage with precision load cell (Methods and Supplementary Figs S7 and S8). The measured percentage change in resistance ( $\Delta R\%$ ) as a function of normal load appears in Fig. 2d, for sensors with three different thicknesses of PDMS and a fixed total thickness. The sensitivity increases with PDMS thickness ( $h$ ), qualitatively consistent with trends in computed values of strain in the PSR bridge (Supplementary Fig. S6b). We also evaluated changes in resistance associated with full inflation of the balloon substrate (similar to images of Fig. 1; up to 130%), as shown in Fig. 2e.

Temperature sensors, like tactile sensors, demand decoupling of the response from in-plane strains; similar design solutions apply. We used a thin, meandering trace of Pt as a resistance-based detector. In geometries shown in Fig. 1d (50 nm Pt), the resistance changes by 1.91  $\Omega\text{ }^\circ\text{C}^{-1}$  (Supplementary Figs S9 and S10a). Typical precision in resistance measurements is  $\sim 0.003\%$ , corresponding to temperature changes of  $\sim 0.03$  °C. Strains can also alter the resistance, but the designs reported here reduce these effects to levels that correspond to shifts in temperature of only  $\sim 1.5$  °C, even for changes in strain ( $\sim 130\%$ ) associated with transformation from completely deflated to fully inflated states of the balloon (as in Fig. 1; see Supplementary Fig. S10b). As with the tactile and other resistance-based sensors described here, the resistance of the interconnects represents a negligible contribution to the measurement.

Temperature is a critical parameter because it provides a way to monitor ablation of aberrant tissue in cardiac arrhythmia treatment. Here, exposed electrode pads (Fig. 2f inset, Supplementary Fig. S11) provide electrical contact directly to the tissue for the purpose of local RF ablation. Variations in temperature both laterally along the surface of the tissue and into its depth determine critical aspects of lesions formed by this ablation process. When combined with quantitative modelling of the ablation process and thermal diffusion, these measurements provide both types of information. To this end, we developed nonlinear models for characterizing electrical and thermal transport, and validated them through comparisons to measurements of in-plane temperature distributions created using a single RF ablation electrode (inset in Fig. 2f) against a piece of tissue from a chicken breast ( $\sim 15$  cm  $\times$  15 cm). For calibration, we used a commercial infrared imaging system (InfraScope Thermal Imager, QFI) to acquire high-resolution temperature maps. A representative measurement appears in Fig. 2f, with an ablation electrode (290  $\times$  560  $\mu\text{m}$ ), and an applied voltage oscillating between +9 and –9 V in a 450 kHz sinusoidal waveform.

Heat released during ablation results from current that flows between the small active electrode and the ground electrode. The distributed Joule heat source  $q$  due to this current is given by  $q = \sigma(T)\nabla V \cdot \nabla V$ , where  $\sigma(T)$  is the temperature-dependent electrical conductivity, and the electric potential  $V$ , corresponding to the root mean square value of the voltage, is determined from  $\nabla \cdot \sigma(T)\nabla V = 0$  (ref. 29). The quasi-stationary electrical equation is adequate for RF ablation, because the tissue can be considered purely resistive at these frequencies (300 kHz–1 MHz; ref. 30). The temperature distribution in the tissue is obtained from the equation<sup>29</sup>  $\rho c(\partial T/\partial t) = \nabla \cdot k\nabla T + \sigma(T)\nabla V \cdot \nabla V - Q_p + Q_m$ , where  $t$ ,  $\rho$ ,  $c$  and  $k$  are the time, mass density, specific heat and thermal



**Figure 2 | Fabrication, characterization and analysis of tactile and temperature sensors and RF ablation electrodes for multifunctional balloon-catheter devices.** **a**, Schematic cross-sectional drawing of a tactile sensor (left) and calculated distributions of strain (right) at the base of the PSR due to inflation of the balloon substrate, for cases with and without an underlying layer of epoxy. **b**, Calculated deformations and distributions of strain in the PSR across the cross-section of a sensor with the layout illustrated in **a**, induced by uniform compression (black arrows). The top two frames show cases with (above) and without (below) a PDMS layer (white). The bottom two frames show magnified views of the strains in the top part of the PSR bridge. **c**, Optical images of a rectangular feature of PDMS between two electrode pads (left) and a fully integrated tactile sensor (right) containing a PSR layer formed on top of the PDMS. The red dashed line indicates the position of the cross-sectional view depicted in **a**. **d**, Percentage change in resistance versus applied pressure for sensors with three different PDMS thicknesses ( $h$ ). **e**, Percentage change in resistance as a function of time during several cycles of inflating and deflating the balloon substrate. **f**, Infrared-camera image of the distribution of temperature in tissue created by activation of an RF ablation electrode (inset). The highest measured temperatures ( $\sim 70^\circ\text{C}$ ) coincide with the location of the electrode. **g**, Temperature distributions determined by coupled thermal and electrical modelling of the ablation process. **h**, Modelling results for thermal distributions along the radial ( $r$ ) and transverse ( $z$ ) directions. **i**, Distributions in both radial and transverse directions for the cross-sectional plane indicated by the blue dashed line in **g**. **j**, Optical image of a flow sensor. **k**, Plot of  $\Delta R\%$ , as a function of flow rate in water, for three different constant-current measurement modes.

conductivity, respectively. The perfusion heat loss  $Q_p$  and metabolic heat generation  $Q_m$  are negligible for cardiac ablation<sup>29</sup>. Finite-element modelling (ABAQUS) was used to evaluate these coupled, nonlinear partial differential equations. For chicken breast, the thermal conductivity  $k = 0.4683 \text{ W m}^{-1} \text{ }^\circ\text{C}^{-1}$  (ref. 31), and electrical conductivity  $\sigma = 0.80, 1.08, 1.33$  and  $1.58 \text{ S}^{-1} \text{ m}^{-1}$  at 20, 40, 60 and  $80^\circ\text{C}$ , respectively<sup>32</sup>. At steady state, a voltage  $V_0 = 6.1 \text{ V}$  gives a maximum temperature of  $70^\circ\text{C}$  and an in-plane distribution (Fig. 2g) that are consistent with experiment (Fig. 2f). Figure 2h shows the temperature distributions along the radial and thickness directions, which can be used to estimate the lesion size and depth. For a representative temperature  $45^\circ\text{C}$  (ref. 33), the lesion size (diameter) is 1.6 mm, and lesion depth is 0.8 mm (Fig. 2i). The approximately axisymmetric nature of the system, together with treatment of the tissue as an object of semi-infinite object size, enables an analytical modelling, if we ignore the temperature dependence of the electrical conductivity (see Supplementary Figs S12–S14 and Supplementary Information).

Devices similar to those for temperature sensing can quantify near-surface rates of blood flow. In operation, current that passes through a thin metal film creates a small increase in temperature

quantified by measuring the resistance. Any change in the rate of fluid flow over the device (or through tissue contacting the device) changes the steady-state temperature and, thus, the resistance. Figure 2j shows a device with a geometry similar to but larger than that of the temperature sensor of Fig. 1d. The data of Fig. 2k illustrate the response as a function of flow rate when operating in a constant-current mode, for three different currents (50, 75 and 100 mA) corresponding to temperatures of  $24.9^\circ\text{C}$ ,  $30.2^\circ\text{C}$  and  $35.9^\circ\text{C}$ , respectively (Supplementary Fig. S10e). The resistance decreases monotonically with increasing flow rate, with a sensitivity that improves with increasing current. For surgical applications, the temperature must not exceed  $\sim 40^\circ\text{C}$  (ref. 34) to prevent overheating and uncontrolled tissue damage. This consideration suggests that the 50 mA operating condition is most suitable. Devices with layouts identical to those for the temperature sensors (Fig. 1d) show similar responses, as indicated in Supplementary Fig. S10c,d.

Electrophysiological sensors consist of uniform metal pads at nodes of the mesh (Fig. 2f inset), using the same design configuration as the aforementioned RF ablation electrodes. Successful integration of light-emitting diodes onto the same platform (Fig. 1e) demonstrates that active semiconductor devices

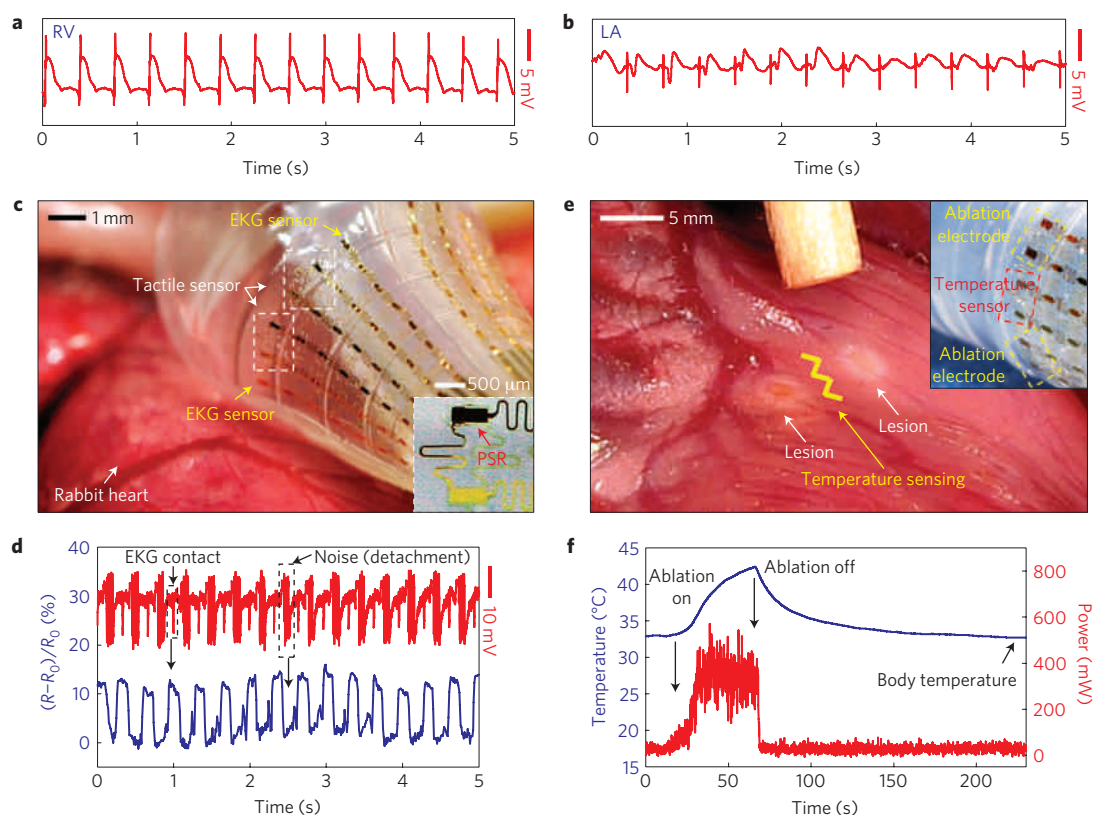


**Figure 3** | *In vivo* epicardial recordings of cardiac electrophysiological, tactile and temperature data, and RF ablation in a rabbit heart. **a**, Epicardial activation map of the RV. The ‘spike and dome’ configuration indicates elevated S–T segments with  $\sim 25$  ms duration. **b**, Electrical mapping of LA activity. **c**, Optical image of an instrumented balloon catheter in its inflated state, showing an array of tactile (white dashed boxes) and electrogram sensors positioned in direct contact with the surface of the RV. The inset shows a magnified view of a tactile sensor. **d**, Simultaneous recordings of electrical activation and mechanical contact measured on the surface of the beating heart. **e**, Optical image of epicardial ablation lesions (white discoloration) created by two pairs of RF ablation electrodes. The yellow line denotes the region of temperature sensing. The inset shows an image of representative RF electrodes collocated with temperature sensors. **f**, Temperature monitoring before, during and after RF ablation. The time constants for the temperature rise and the absolute temperatures achieved during ablation are comparable to those associated with conventional cardiac ablation catheters.

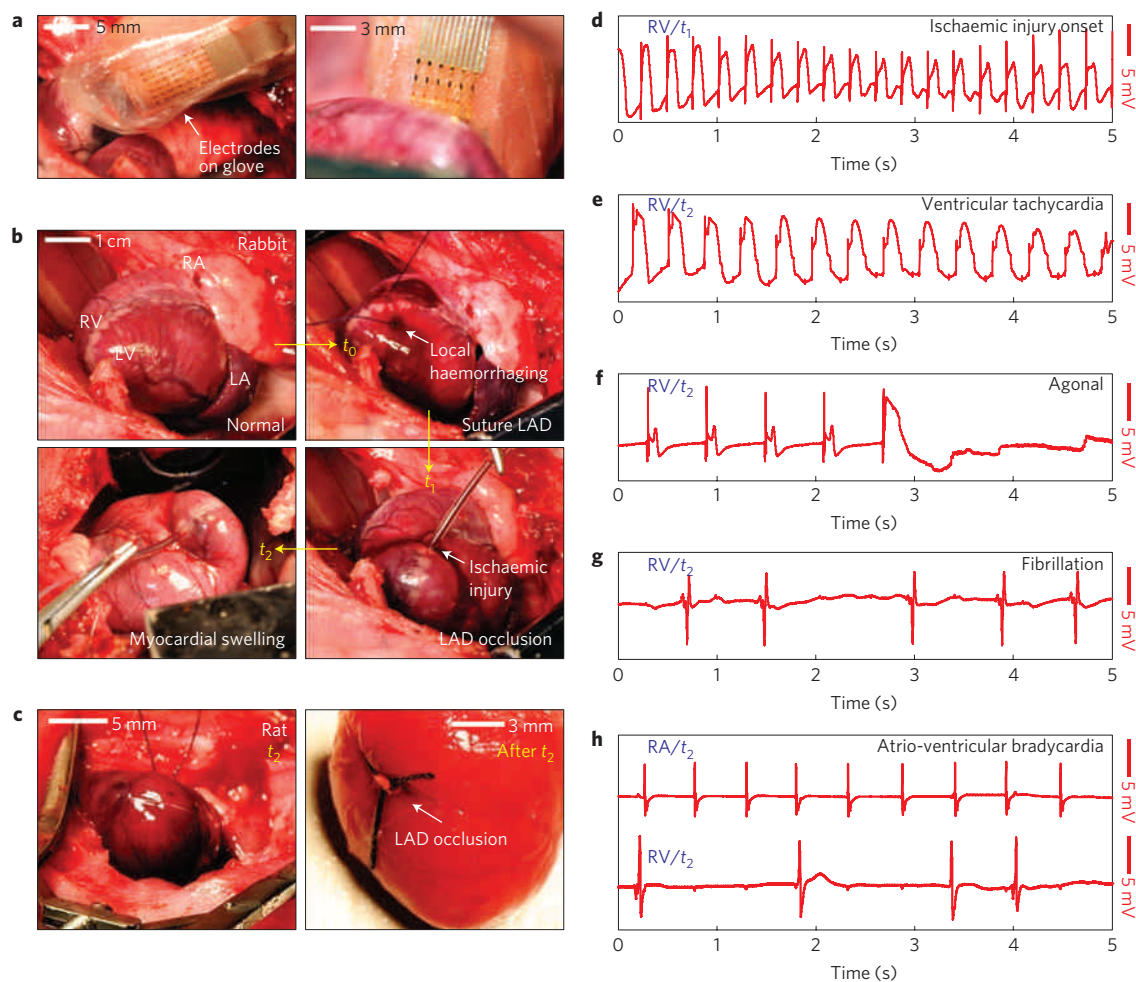
can also be incorporated. The overall concepts, then, provide a path for integrating nearly any class of sensor or semiconductor device onto the balloon, to match requirements for a variety of predicted uses in surgery and diagnostics. In the following, we examine cardiac ablation therapy. Although balloon catheters are optimally suited for endocardial modes (Fig. 1f), evaluating the sensor and ablation functionalities is most easily accomplished through epicardial experiments. The results highlight the ability of the electronics to survive clinically relevant, moist, dynamically changing biological substrates. *In vivo* experiments were carried out on rat and rabbit models in which the heart was surgically exposed following a longitudinal sternotomy and pericardiotomy (see Methods). In each experiment, epicardial electrograms<sup>35</sup> were recorded from balloon-mounted devices with between 2 and 13 bipolar electrodes. The electrodes were typically positioned on the anterior surface of the heart with millimetre placement accuracy using a micromanipulator stage.

Figure 3a,b shows representative recordings ( $\sim 1$  mm spacing between electrodes) on the anterior right ventricle (RV) and the left atrium (LA) surfaces. Each electrocardiogram was obtained by differentiating potential readings from one pair of electrodes. The noise levels were  $\sim 10$   $\mu$ V, corresponding to signal-to-noise ratios of 60 dB. The electrodes have impedances of  $26$  k $\Omega \pm 8\%$  at 1 kHz, measured while immersed in normal saline (0.9%) solution. The RV response (Fig. 3a) reveals an S–T segment in an elevated ‘spike and dome’ shape similar to that of monophasic action potentials. In contrast, the recordings from the LA (Fig. 3b) exhibited different

electrogram shapes, demonstrating the ability of a high-density electrode array on a balloon to capture significant features of epicardial activation from different regions of the heart.

The representative S–T elevation recorded from the RV was found at multiple sites along the anterior RV and across the anterior basal regions of the LV. This feature is probably induced by pressure exerted on the surface of the heart<sup>35</sup>. The instrumented balloon-catheter system thus provides a route for minimizing inflation-induced injuries by evaluating S–T elevation recordings from balloon electrodes. This concept can be applied to endocardial measurements in the pulmonary veins, where contact pressures exerted during inflation are not well understood. Therefore, we can determine the necessary amount of inflation required to make contact with heart tissue without causing significant damage during inflation using electrical recordings on the balloon surface.

An alternative way to monitor balloon-inflation levels and electrical contact is to use tactile sensors on the balloon. These sensors provide accurate feedback about the contact between the heart and the devices (Fig. 3c,d). Figure 3d shows that the tactile sensor can be used to track clean contact from detachment on a cycle-by-cycle basis without significant hysteresis. In Fig. 3d, the percentage change of resistance recorded from the tactile sensor (blue) clearly correlates with the electrogram signal (red). When the balloon was in good contact, high-quality electrical activation signals were measured, whereas noisy signals were obtained when the balloon was detached from the heart surface. Because these sensors have sufficient sensitivity for tracking normal sinus rhythm



**Figure 4 | In-vivo epicardial mapping of electrophysiology using an instrumented surgical glove during ischaemic injury.** **a**, Optical image of a smart surgical glove in close proximity to the beating heart. **b**, Series of images documenting the progression of ischaemic injury induced by surgical occlusion of the LAD coronary artery with a suture in a rabbit heart. Haemorrhaging was followed by myocyte apoptosis and necrotic cell death  $\sim 15$ – $20$  min later. The heart became visibly enlarged, indicating significant fluid retention, swelling of cardiac myocytes and oedema, particularly in the ischaemic region. A simultaneous reduction in cardiac output was observed. **c**, Optical image showing effects of ischaemic injury in a rat heart using the same approach. **d**, Electrogram of epicardial activation near the RV immediately following LAD occlusion ( $t_1$ ). **e**, S-T elevation was noticeable at  $t_2 \approx 5$  min with slight increase in sinus rhythm pace ( $\sim 260$  bpm). At  $t_2 \approx 15$  min, the shape of electrical activation was consistent with ventricular tachycardia. The large dome shapes indicate S-T segment elevation beyond levels in Fig. 1d. **f**, Electrogram showing the heart in agonal phase, marked by very slow erratic beating ( $t_2 \approx 30$  min). **g**, Atrial fibrillation was also apparent, marked by erratic *p*- and *t*-wave behaviour between QRS complexes. **h**, Surface activation from the RV and the RA was detected simultaneously using an array of sensors on a surgical glove.

at  $\sim 240$  bpm, we expect that they can be used to detect onset of tachycardias in humans to evaluate the mechanical heart rhythm. We note that temperature changes associated with motion in and out of contact with the tissue can contribute to the pressure response. Collocated temperature sensors indicated that these differences were less than  $1^\circ\text{C}$  for beat rates of  $0.5 \sim 2$  Hz; from Supplementary Fig. S9, these changes correspond to resistance variations of less than  $0.5\%$  in the tactile sensors.

We also tested the ability of our RF ablation electrodes to create lesions on the heart (Fig. 3e). Ablation using multiple electrodes simultaneously to form larger lesions is also possible (Supplementary Fig. S11a). These devices were coupled with temperature sensors to monitor the extent of lesion formation (Fig. 3e). The temperature recording shows the same pattern with input RF power change (Fig. 3f). These two devices enable controllable lesion formation. Additional irrigation mechanisms are also possible through microfluidic channel outlets that deliver saline near the ablation electrodes to help avoid charring on the electrodes. In this context and others, flow sensors can be

useful. The transmural extent of typical lesions was evaluated using postoperative analysis, which revealed lesion depths spanning  $1 \sim 5$  mm. We did not observe device degradation due to the presence of biological fluids or mechanical stresses during these ablation or sensing measurements. The PDMS and PI encapsulation layers helped to ensure a robust biocompatible interface, consistent with their use in other contexts described in previous reports<sup>36,37</sup>.

The same concepts as enable instrumentation on balloons can be used with other important platforms of interest such as surgical gloves (Fig. 4a and Supplementary Fig. S15) for open-heart procedures in which concomitant mapping and ablation steps are required. A clinical demonstration is highlighted in Fig. 4b,c, in which an induced ischaemic injury<sup>38</sup> caused by occlusion of the lateral anterior descending (LAD) coronary artery is monitored in real time. The electrogram waveforms reflect the progression of ischaemic injury from the onset ( $t_0, t_1$ ) to highly elevated S-T segments<sup>35</sup>, followed by a shift to an agonal response marked by very slow heart rate ( $t_2$ ; Fig. 4d–f). These measurements were robust and stable to capture epicardial activity at multiple sites before, during

and after onset of coronary occlusion. Figure 4g,h shows epicardial electrical recordings taken concurrently at multiple anterior sites in the rat model. The electrogram signals recorded from the RA and RV indicate that the cardiac rhythm is ectopic and asynchronous. Supplementary Fig. S15c shows the pressure measurement from a representative tactile sensor on a glove (Supplementary Fig. S15b). Manoeuvring these sensors on the fingertips with natural tactile feedback (from the sense of touch) is also useful for exploring areas of the posterior myocardium, which are out of plain view and consequently difficult to probe during cardiac surgical procedures.

The materials and mechanics concepts introduced here represent a technology foundation for advanced, minimally invasive surgical and diagnostic tools, with demonstrated examples in diagnosing and resolving complex arrhythmogenic disease states of the heart. These devices constitute significant advances over existing balloon and multielectrode catheters in the number of sensing modalities and the spatial density of sensors. Related ideas should also be valuable in other contexts, including atherosclerosis, oesophageal and gastro-intestinal diseases, and endometrial and bladder dysfunction, all of which can be addressed using multifunctional, instrumented balloon-catheter systems.

## Methods

**Fabrication of stretchable electrode array.** The fabrication begins with spin coating of a thin film of PI (~1.2  $\mu\text{m}$ , Sigma Aldrich) on a sacrificial layer of poly(methylmethacrylate) (100 nm, MicroChem). Metal-evaporation (Cr/Au, 5 nm/150 nm), photolithography and wet-etching steps define metal electrodes with serpentine-shaped interconnects and rectangular electrodes. Additional PI spin coating, oxygen reactive ion etching and metal deposition for contacts completes the array, as shown in Supplementary Fig. S1a.

**Fabrication and compression test of tactile sensors.** After patterning serpentine interconnects and electrodes (Cr/Au, 5/150 nm) on a uniform thin sheet of PI (1.2  $\mu\text{m}$  thick), casting procedures form a rectangular feature of PDMS (160  $\mu\text{m}$   $\times$  220  $\mu\text{m}$ ) between two adjacent Au electrode pads (150 nm thick; left frame, Fig. 2c). Similar steps define a bridge-shaped structure of PSR (160  $\mu\text{m}$   $\times$  430  $\mu\text{m}$ ) that passes over the PDMS and covers the pads on both sides. Patterning casting procedures form the required features of PDMS and PSR. Here, photolithography first creates trenches in a thick layer of photoresist (AZ P4620, AZ Electronic Materials). Spin coating PDMS (20:1 mixture of base to curing agent; Sylgard 184, Dow Corning) on top of this resist, curing it at 70 °C for 1 h and then etching back the PDMS removes any residual material from the top surface of the resist. Rinsing with acetone washes away the resist. Next, similarly patterned AZ P4620 defines a structure for the required features of PSR (Elastosil LR 3162, Wacker Silicones). In this case, placing an excess of this material on top of the resist and then scraping with a razor blade forces it into the trenches and removes it from adjacent areas. Curing at 70 °C for 1 h and then removing the resist yields the desired PSR structure. The tactile sensor is completed by spin-casting a layer of PI for encapsulation.

To calibrate the response, the entire structure is transfer printed onto a 1-mm-thick slab of PDMS (30:1 mixture of base to curing agent). A multimeter (SMU2055, Signametrics) measures the change in resistance during compression using a custom assembly of stages and a 25-g-force GSO load cell (Transducer Techniques) fixed on a vibration-isolation table, as shown in Supplementary Fig. S7. The indentation head mounts on a support designed to cover a single tactile sensor. The tactile sensor attaches to a glass slide that attaches to a vertical translation stage with positioning accuracy of 1  $\mu\text{m}$ . A microscope above the stage facilitates manual alignment. After bringing the device into slight contact with the indentation head, the sample stage moves downward by 30  $\mu\text{m}$  at a speed of 1  $\mu\text{m s}^{-1}$ . For cyclic fatigue testing, speeds were 120  $\mu\text{m s}^{-1}$ . Slight drift in the baseline response can be significantly reduced by several cycles of compression before testing<sup>39</sup>.

**Fabrication of temperature and flow sensors.** Thin layers of Ti/Pt (5 nm/50 nm) deposited with an electron-beam evaporator serve as the basis for the temperature and flow sensors (Fig. 1d). A lift-off process defines the meandering electrode patterns. Surface treatment of the PI with oxygen plasma or deposition of a thin silicon dioxide (SiO<sub>2</sub>) layer (~50 nm) on top of the PI improves the adhesion of the Pt. Patterning gold interconnects, encapsulating with a layer of PI and etching to define the mesh completes the fabrication.

**Connector fabrication and integration.** The connector consists of an array of metal lines (Cr/Au, 5 nm/150 nm) on a commercial PI film (Kapton, Dupont). Another top coating of PI (~1.2  $\mu\text{m}$ ) helps to prevent breakage or delamination of the metal during integration. The stretchable electrode array and one side of

the connector are interconnected with an ACF, connected through application of heat (~150 °C) and pressure with conventional binder clips for ~10 min, as shown in Supplementary Fig. S5b. The opposite side of the connector connects through the ACF to a circuit board that interfaces to an analog-to-digital converter for data acquisition.

**Animal experiments.** Experiments used rat ( $n = 4$ ; 390–500 g) and rabbit ( $n = 4$ ; 3.5–4.0 kg) models. All rats were anaesthetized with an initial dose of 0.45 ml sodium pentobarbital (Nembutal; 50 mg ml<sup>-1</sup>) supplemented with 0.15 ml (25 mg ml<sup>-1</sup>) booster doses at ~1 h intervals. Rabbits were anaesthetized with a 0.5 ml kg<sup>-1</sup> mixture of ketamine (30 mg kg<sup>-1</sup>), xylazine (7 mg kg<sup>-1</sup>) and acepromazine (3.5 mg kg<sup>-1</sup>), and were then intubated and maintained with 2% isoflurane at room temperature. A median sternotomy and pericardiotomy were carried out to gain access to the epicardium. Next, the parietal pericardium was removed to enable balloon- and sheet-based devices to come in direct contact with the heart. A micromanipulator stage with micrometre-scale accuracy was used to position the balloon-catheter surface in contact with the anterior surface of the heart. Ringer's solution was used to keep the epicardial surface moist during experiments. Measurements were made at multiple sites along the LA, RA, RV and LV surfaces to differentiate local excitation across the different chambers of the heart. During ischaemic-injury experiments (Fig. 4), a suture ligature was used to occlude the LAD coronary artery. Electrocardiograms were recorded with multifunctional devices to capture the onset and development of injury at multiple sites on the heart. All animal experiments were approved by the Institutional Animal Care and Use Committee at the University of Arizona. Endocardial measurements using femoral vein access into the porcine heart (Fig. 1f) were carried out to capture X-ray images using previously published procedures<sup>14</sup>. These experiments were approved by the Massachusetts General Hospital Center for Comparative Medicine.

**Data-acquisition systems.** The data-acquisition system consists of a pressure-sensing module and an electrophysiological-mapping module (Supplementary Fig. S16a). The pressure-sensing circuit sends a controlled programmable current across the tactile pressure sensor's terminals. The AD8671 operational amplifier generates the constant current. A switch toggles between two current ranges (Supplementary Fig. S16b). Voltage changes across the tactile pressure sensor are monitored by an NI PXI-6289 and PXIe-10731 data acquisition board.

The electrophysiological signals detected by the stretchable electrode array are conditioned with the Intan RHA1016, a multiplexed biopotential amplifier array. The RHA1016 provides common-mode rejection, gain, low-pass filtering at 5 kHz and multiplexing. A Ripple Grapevine system converts the multiplexed analog signal from the RHA1016 to digital output. It samples the RHA1016's output at 300 kpsps and decimates the signal to 1 kpsps. In addition, it applies a digital 50/60 Hz notch filter to the signal. The data are recorded in the Cyberkinetics NEV2.2 NS2 format. The data are then viewed with custom Matlab software.

Received 3 November 2010; accepted 25 January 2011;  
published online 6 March 2011

## References

- Mueller, R. & Sanborn, T. The history of interventional cardiology. *Am. Heart J.* **129**, 146–172 (1995).
- Myler, R. & Stertz, S. *Textbook of Interventional Cardiology* Ch. 12 (WB Saunders, 1993).
- Rich, S., Dodin, E. & McLaughlin, V. V. Usefulness of atrial septostomy as a treatment for primary pulmonary hypertension and guidelines for its application. *Am. J. Cardiol.* **80**, 369–371 (1997).
- Rothman, A. *et al.* Graded balloon dilation atrial septostomy as a bridge to lung transplantation in pulmonary hypertension. *Am. Heart J.* **125**, 1763–1766 (1993).
- Aliot, E. M. *et al.* Expert consensus statement on catheter and surgical ablation of atrial fibrillation: Recommendations for personnel, policy, procedures and follow-up, a report of the heart rhythm society (HRS) task force on catheter and surgical ablation of atrial fibrillation. *Europace* **9**, 335–379 (2007).
- Calkins, H. *et al.* Treatment of atrial fibrillation with antiarrhythmic drugs for radio frequency ablation: Two systematic literature reviews and meta-analyses. *Circ. Arrhythmia Electrophysiol.* **2**, 349–361 (2009).
- Dewire, J. & Calkins, H. State-of-the-art and emerging technologies for atrial fibrillation ablation. *Nature Rev. Cardiol.* **7**, 129–138 (2010).
- Chun, K. R. *et al.* The 'single big cryoballoon' technique for acute pulmonary vein isolation in patients with paroxysmal atrial fibrillation: A prospective observational single centre study. *Euro. Heart J.* **30**, 699–709 (2009).
- Chun, K. R. *et al.* Cryoballoon pulmonary vein isolation with real time recordings from the pulmonary veins. *J. Cardiovasc. Electrophysiol.* **30**, 699–709 (2009).
- Satake, S. *et al.* Usefulness of a new radiofrequency thermal balloon catheter for pulmonary vein isolation: A new device for treatment of atrial fibrillation. *J. Cardiovasc. Electrophysiol.* **14**, 609–615 (2003).

11. Schmidt, B. *et al.* Pulmonary vein isolation by high intensity focused ultrasound: First in-man study with a steerable balloon catheter. *Heart Rhythm*. **4**, 575–584 (2007).
12. Reddy, V. Y. *et al.* Visually-guided balloon catheter ablation of atrial fibrillation: Experimental feasibility and first in-human multicenter clinical outcome. *Circulation* **120**, 12–20 (2009).
13. Reddy, V. Y. *et al.* Balloon catheter ablation to treat paroxysmal atrial fibrillation: What is the level of venous isolation? *Heart Rhythm*. **5**, 353–360 (2008).
14. Mansour, M. *et al.* Initial experience with the Mesh catheter for pulmonary vein isolation in patients with paroxysmal atrial fibrillation. *Heart Rhythm*. **5**, 1510–1516 (2008).
15. Meissner, A. *et al.* First experiences for pulmonary vein isolation with the high density mesh ablator (HDMA): A novel mesh electrode catheter for both mapping and radiofrequency delivery in a single unit. *J. Cardiovasc. Electrophysiol.* **20**, 359–366 (2009).
16. Lau, M. *et al.* A theoretical and experimental analysis of radiofrequency ablation with a multielectrode, phased, duty-cycled system. *PACE* **33**, 1089–1100 (2010).
17. Di Biase, L. *et al.* Relationship between catheter forces, lesions, characteristics, popping and char formation: Experience with robotic navigation system. *J. Cardiovasc. Electrophysiol.* **20**, 436–440 (2009).
18. Kim, D-H. *et al.* Materials and noncoplanar mesh designs for integrated circuits with linear elastic responses to extreme mechanical deformations. *Proc. Natl Acad. Sci. USA* **105**, 18675–18680 (2008).
19. Viventi, J. *et al.* A Conformal, bio-interfaced class of silicon electronics for mapping cardiac electrophysiology. *Sci. Translational Med.* **2**, 24ra22 (2010).
20. Kim, R-H. *et al.* Waterproof AlInGaP optoelectronics on stretchable substrates with applications in biomedicine and robotics. *Nature Mater.* **9**, 929–937 (2010).
21. Mathura, A. B., Collinsworth, A. M., Reichert, W. M., Kraus, W. E. & Truskey, G. A. Endothelial, cardiac muscle and skeletal muscle exhibit different viscous and elastic properties as determined by atomic force microscopy. *J. Biomechanics*. **34**, 1545–1553 (2001).
22. Lee, M. H. & Nicholls, H. R. Tactile sensing for mechatronics—a state of the art survey. *Mechatronics* **9**, 1–31 (1999).
23. Dargahi, J., Parameswaran, M. & Payandeh, S. A micromachined piezoelectric tactile sensor for an endoscopic grasper—theory, fabrication and experiments. *J. Microelectromech. Syst.* **9**, 329–335 (2000).
24. Engel, J., Chen, J. & Liu, C. Development of polyimide flexible tactile sensor skin. *J. Micromech. Microeng.* **13**, 359–366 (2003).
25. Someya, T. *et al.* A large-area, flexible pressure sensor matrix with organic field-effect transistors for artificial skin applications. *Proc. Natl Acad. Sci. USA* **101**, 9966–9970 (2004).
26. Takei, K. *et al.* Nanowire active-matrix circuitry for low-voltage macroscale artificial skin. *Nature Mater.* **9**, 821–826 (2010).
27. Kim, D-H. *et al.* Optimized structural designs for stretchable silicon integrated circuits. *Small* **5**, 2841–2847 (2009).
28. Sun, J-Y. *et al.* Inorganic islands on a highly stretchable polyimide substrate. *J. Mater. Res.* **24**, 3338–3342 (2009).
29. Berjano, E. J. Theoretical modelling for radiofrequency ablation: State-of-the-art and challenges for the future. *Biomed. Eng. Online* **5**, 24 (2006).
30. Plonsey, R. & Heppner, D. B. Considerations of quasi-stationarity in electrophysiological systems. *Bul. Math. Biophys.* **29**, 657–664 (1967).
31. Huang, L. & Liu, L. Simultaneous determination of thermal conductivity and thermal diffusivity of food and agricultural materials using a transient plane-source method. *J. Food Eng.* **95**, 179–185 (2009).
32. Zell, M., Lyng, J. G., Cronin, D. A. & Morgan, D. J. Ohmic heating of meats: Electrical conductivities of whole meats and processed meat ingredients. *Meat. Sci.* **83**, 563–570 (2009).
33. Erez, A. & Shitzer, A. Controlled destruction and temperature distribution in biological tissues subjected to monoactive electrocoagulation. *J. Biomed. Eng.* **102**, 42–49 (1980).
34. Jiang, G. & Zhou, D. D. in *Implantable Neural Prostheses 2, Biological and Medical Physics* (eds Zhou, D. D. & Greenbaum, E.) Ch. 2, 27–61 (Springer, 2010).
35. Machi, E. *et al.* High density epicardial mapping during current injection and ventricular activation in rat hearts. *Am. J. Heart Circ. Physiol.* **275**, H1886–H1897 (1998).
36. Bélanger, M. C. & Marois, Y. Hemocompatibility, biocompatibility, inflammatory and *in vivo* studies of primary reference materials low-density polyethylene and polydimethylsiloxane: A review. *J. Biomed. Mater. Res.* **58**, 467–477 (2001).
37. Richardson, R. R. Jr, Miller, J. A. & Reichert, W. M. Polyimides as biomaterials: Preliminary biocompatibility testing. *Biomaterials* **14**, 627–635 (1993).
38. Wit, A. L. & Janse, M. J. Experimental models of ventricular tachycardia and fibrillation caused by ischemia and infarction. *Circulation* **85**, I-32–I-42 (1992).
39. Shin, M. K. *et al.* Elastomeric conductive composites based on carbon nanotube forests. *Adv. Mater.* **22**, 2663–2667 (2010).

### Acknowledgements

We thank K. Dowling for help in high-resolution imaging and analysis of devices. We thank B. Dehdashti and members of the Sarver Heart Center for help in preparing the animals for *in vivo* studies. We thank S. Laferriere and the Massachusetts General Hospital Electrophysiology Laboratory for help with X-ray imaging in animals. This material is based on work supported by the National Science Foundation under grant DMI-0328162 and the US Department of Energy, Division of Materials Sciences, under award DE-FG02-07ER46471, through the Materials Research Laboratory and Center for Microanalysis of Materials (DE-FG02-07ER46453) at the University of Illinois at Urbana-Champaign. N.L. acknowledges support from a Beckman Institute postdoctoral fellowship. J.A.R. acknowledges a National Security Science and Engineering Faculty Fellowship.

### Author contributions

D-H.K., N.L., R.G. and J.A.R. designed the experiments. D-H.K., N.L., R.G., Y-S.K., S.P.L., L.X., J.W., R-H.K., J.S., Z.L., B.D.G., B.E., M.J.S., S.H., J.V., J.D.M., S-M.W., Y.H., B.L. and J.A.R. carried out experiments and analysis. D-H.K., N.L., R.G., M.M., M.J.S., J.S., Y.H. and J.A.R. wrote the paper.

### Additional information

The authors declare competing financial interests: details accompany the paper at [www.nature.com/naturematerials](http://www.nature.com/naturematerials). Supplementary information accompanies this paper on [www.nature.com/naturematerials](http://www.nature.com/naturematerials). Reprints and permissions information is available online at <http://ngp.nature.com/reprintsandpermissions>. Correspondence and requests for materials should be addressed to J.A.R.

# Materials for multifunctional balloon catheters with capabilities in cardiac electrophysiological mapping and ablation therapy

Dae-Hyeong Kim<sup>1,†</sup>, Nanshu Lu<sup>1,†</sup>, Roozbeh Ghaffari<sup>2,†</sup>, Yun-Soung Kim<sup>1</sup>, Stephen P. Lee<sup>2</sup>, Lizhi Xu<sup>1</sup>, Jian Wu<sup>3</sup>, Rak-Hwan Kim<sup>1</sup>, Jizhou Song<sup>4</sup>, Zhuangjian Liu<sup>5</sup>, Jonathan Viventi<sup>6</sup>, Bassel de Graff<sup>2</sup>, Brian Elolampi<sup>2</sup>, Moussa Mansour<sup>7</sup>, Marvin J. Slepian<sup>8</sup>, Sukwon Hwang<sup>1</sup>, Joshua D. Moss<sup>9</sup>, Sang-Min Won<sup>1</sup>, Younggang Huang<sup>3</sup>, Brian Litt<sup>6,10</sup>, John A. Rogers<sup>1\*</sup>

<sup>1</sup>*Department of Materials Science and Engineering, Beckman Institute for Advanced Science and Technology, and Frederick Seitz Materials Research Laboratory, University of Illinois at Urbana-Champaign, Urbana, IL 61801 USA*

<sup>2</sup>*MC10 Inc., 36 Cameron Avenue, Cambridge, MA 02140 USA*

<sup>3</sup>*Department of Mechanical Engineering and Department of Civil and Environmental Engineering, Northwestern University, Evanston, IL 60208*

<sup>4</sup>*Department of Mechanical and Aerospace Engineering, University of Miami, Coral Gables, FL 33146, USA*

<sup>5</sup>*Institute of High Performance Computing, 1 Fusionopolis Way, #16-16 Connexis, Singapore 138632.*

<sup>6</sup>*Department of Bioengineering, University of Pennsylvania, Philadelphia, PA 19104 USA*

<sup>7</sup>*Massachusetts General Hospital, Harvard Medical School, Boston, MA 02114 USA*

<sup>8</sup>*Sarver Heart Center, University of Arizona, Tucson, AZ 85724 USA*

<sup>9</sup>*Department of Cardiology, Hospital of the University of Pennsylvania, 9 Founders Pavilion, 3400 Spruce Street, Philadelphia, PA 19104 USA*

<sup>10</sup>*Department of Neurology, Hospital of the University of Pennsylvania, 3 West Gates, 3400 Spruce Street, Philadelphia, PA 19104 USA*

<sup>†</sup>*D.-H. Kim, N. Lu and R. Ghaffari contributed equally.*

*\*To whom correspondence should be addressed. E-mail: jrogers@uiuc.edu*

**Analytical model to determine the shape of catheter**

The expanded catheter can be well represented by (part of) an ellipse. Its semi-minor axis is the maximum radius  $r$  of the expanded catheter, and the semi-major axis is determined by requiring the ellipse to pass through the end cross section as  $L/\left(2\sqrt{1-R^2/r^2}\right)$ , where  $L, R$  are the length and initial radius of the catheter. The force equilibrium on the expanded catheter then gives the axial strain in the catheter by

$$\varepsilon_{\text{axial}} = \frac{pR}{Eh} \left[ \sqrt{\frac{r^2}{R^2} - \left(\frac{r^2}{R^2} - 1\right)\xi^2} - 1 \right] f\left(\xi, \lambda, \frac{r}{R}\right) \tag{S1}$$

where  $p$  is the internal pressure,  $E$  is the Young’s modulus,  $h$  is the thickness of the catheter,  $\lambda=2R/L$  and  $\xi=2z/L$  are the aspect ratios,  $z$  is the coordinate along the axial direction with

the origin at the catheter center, and  $f(\xi, \lambda, r/R) = \sqrt{1 + \frac{\lambda^2 (r^2/R^2 - 1)^2 \xi^2}{r^2/R^2 - (r^2/R^2 - 1)\xi^2}}$ . By requiring

the vanishing elongation along the axial direction between the two end cross sections, the normalized internal pressure is given by.

$$\frac{pR}{Eh} = \frac{\int_0^1 f\left(\xi, \lambda, \frac{r}{R}\right) d\xi - 1}{\int_0^1 f^2\left(\xi, \lambda, \frac{r}{R}\right) \left[ \sqrt{\frac{r^2}{R^2} - \left(\frac{r^2}{R^2} - 1\right)\xi^2} - 1 \right] d\xi} \tag{S2}$$

The displacements of the catheter in the axial and radial directions, which determine the strains in islands and serpentine bridges, are given by

$$u_{axial} = z - \frac{L}{2} \int_0^{2z/L} f\left(\xi, \lambda, \frac{r}{R}\right) d\xi + \frac{pR}{Eh} \frac{L}{2} \int_0^{2z/L} f^2\left(\xi, \lambda, \frac{r}{R}\right) \left[ \sqrt{\frac{r^2}{R^2} - \left(\frac{r^2}{R^2} - 1\right)\xi^2} - 1 \right] d\xi, \quad (S3)$$

$$u_{radial} = \sqrt{r^2 - 4\left(r^2 - R^2\right)\frac{z^2}{L^2}} - R. \quad (S4)$$

Figure S1a shows that the above analytical solutions agree well with the finite element analyses without any parameter fitting. Therefore, the above expressions can be used to determine the deformation of serpentine bridges on the expanded catheter.

### Finite element model to determine the strains in bridges and islands

The finite element method (FEM) is used to determine the strain distributions in serpentine bridges and islands. Eight-node, hexahedral brick elements (C3D8) in the finite element analysis software ABAQUS (2009) are used for the substrate, which is modeled as a hyper-elastic material. Four-node, multi-layer shell elements (S4R) are used for the islands and serpentine bridges, which are linear elastic. The islands are bonded to the substrate by sharing the nodes, but the serpentine bridges do not. Figure S1b shows the position of island on the expand catheter, while the strains, which may reach 130%, in the expand catheter are shown in Fig. S1c. Figure S2a shows strain contour on top, middle and bottom layer of the bridge. The strains are below 1% due to the buckling of the bridges. The strains in the middle layer of temperature and tactile sensors are shown in Fig. S2b.

### Thermal modelling to determine the temperature on the tissue

The temperature on the tissue has been obtained analytically in Eq. (1) by neglecting the temperature dependence of the electrical conductivity. Figure S12 shows the

effect of the coefficient of natural convection ( $h$ ) on the temperature distribution along radial and thickness directions. The case with the maximum  $h$  ( $25\text{W/m}^2/\text{°C}$ ) predicts  $\sim 2.5$   $\text{°C}$  higher than the case with  $h = 0$ , which shows that the convection boundary can be approximated by adiabatic boundary. The non-dimensional function  $\bar{\theta}$  in the analytical expression of temperature on the issue is then independent of material properties and shown in Fig. S13a. Figure S13b shows  $\bar{\theta}$  versus  $z/r_0$  at  $r = 0$  as well as the fitted curve

$$\bar{\theta}\left(0, \frac{z}{r_0}\right) \approx 0.00166 + 0.08486e^{-0.06526\frac{z}{r_0}} + 0.42337e^{-0.43999\frac{z}{r_0}}. \quad (\text{S5})$$

Figure S13c shows  $\bar{\theta}$  versus  $r/r_0$  at  $z = 0$  and the fitted curve is

$$\bar{\theta}\left(\frac{r}{r_0}, 0\right) \approx \begin{cases} 0.48 & 0 \leq \frac{r}{r_0} \leq 1 \\ 0.00375 + 0.71836e^{-0.77808\frac{r}{r_0}} + 0.15451e^{-0.11234\frac{r}{r_0}} & \frac{r}{r_0} > 1 \end{cases}. \quad (\text{S6})$$

Figure S13a, together with Eqs. (S5) and (S6) are very useful to estimate the lesion size and depth if the temperature to form lesion is known.

The analytical model with an equivalent, temperature independent electrical conductivity  $\sigma_{eq} = 0.970 \text{ s/m}$  is compared to the finite element simulations with temperature dependent electrical conductivity in Fig. S14a and S14b.  $\sigma_{eq}$  is equal to the thermal conductivity corresponding to the half value of the highest temperature obtained by finite

element simulations. The analytical results yield a good agreement with FEM. The analytical model can also be used to determine the temperature distribution if the temperature at some specified location is known. Figure 14c shows the temperature distribution between two electrodes (red dots) based on the temperature at the location (blue dot) of temperature sensor by neglecting the interaction between two electrodes.

### Analytical modelling to determine the temperature distribution

The Laplace equation for electric potential is  $\frac{\partial^2 V}{\partial r^2} + \frac{1}{r} \frac{\partial V}{\partial r} + \frac{\partial^2 V}{\partial z^2} = 0$  in the radial and axial coordinates  $(r, z)$ . The boundary condition on the surface  $z=0$  is  $V = V_0$  for  $0 \leq r \leq r_0$  and  $-\sigma \frac{\partial V}{\partial z} = 0$  for  $r > r_0$ , where  $r_0$  is the half size of the active electrode. The remote boundary condition is  $V = 0$  for  $r \rightarrow \infty$  or  $z \rightarrow \infty$ . The electric potential can be obtained analytically as  $V = \frac{2V_0}{\pi} \arcsin \left( \frac{2}{\sqrt{(r/r_0 - 1)^2 + (z/r_0)^2} + \sqrt{(r/r_0 + 1)^2 + (z/r_0)^2}} \right)$ . For the steady-state solution, the temperature satisfies  $\frac{\partial^2 T}{\partial r^2} + \frac{1}{r} \frac{\partial T}{\partial r} + \frac{\partial^2 T}{\partial z^2} + \frac{\sigma \nabla V \cdot \nabla V}{k} = 0$  and boundary conditions  $-k \frac{\partial T}{\partial z} = -h(T - T_\infty)$  on the surface  $z = 0$  and  $T = T_\infty$  for  $r \rightarrow \infty$  or  $z \rightarrow \infty$ , where  $h$  ( $2 \sim 25$  W/m<sup>2</sup>/k) is the coefficient of natural convection. For a constant  $\sigma$ , the temperature is obtained analytically as

$$T = \frac{\sigma V_0^2}{k} \bar{\theta} \left( \frac{r}{r_0}, \frac{z}{r_0}, \frac{r_0 h}{k} \right) + T_\infty, \quad (\text{S7})$$

where  $\bar{\theta}$  is a non-dimensional function of normalized positions  $r/r_0$  and  $z/r_0$ . It depends very weakly on the dimensionless thermal property  $r_0 h/k$  (error  $\sim 2^\circ\text{C}$ , confirmed by finite element analysis shown in Fig. S12), and is given by

$$\bar{\theta}\left(\frac{r}{r_0}, \frac{z}{r_0}\right) = \frac{2}{\pi^3} \frac{r}{\sqrt{r_0}} \int_{\eta=0}^{\infty} \sqrt{\eta} \int_{\xi=0}^{\infty} \frac{Q_{-\frac{1}{2}}\left[\frac{(z/r_0 - \xi)^2 + \eta^2 + (r/r_0)^2}{2\eta r/r_0}\right] + Q_{-\frac{1}{2}}\left[\frac{(z/r_0 + \xi)^2 + \eta^2 + (r/r_0)^2}{2\eta r/r_0}\right]}{\left[\sqrt{(\eta-1)^2 + \xi^2} + \sqrt{(\eta+1)^2 + \xi^2}\right]^2 \sqrt{(\eta-1)^2 + \xi^2} \sqrt{(\eta+1)^2 + \xi^2}} d\xi d\eta \tag{S8}$$

where  $Q$  is the Legendre Function of 2<sup>nd</sup> kind. The function  $\bar{\theta}$  in Eq. (S8) does not depend on any material parameters, and is shown in Fig. S13. This framework, with the same values for  $r_0$ ,  $k$ ,  $V_0$  as for the numerical modelling, but with an equivalent, temperature independent electrical conductivity of 0.970 S/m, yields results that are remarkably consistent with modelling and experiment (Fig. S14). The analytical forms can be helpful in examining different functional dependencies.

**SI Figure Caption**

**Figure S1. a**, Plot of balloon displacement vs axial position that shows good agreement between an analytical solution and finite element analysis. **b**, Estimation of the position of

each island during inflation and deflation, evaluated by finite element analysis. **c**, Longitudinal (left) and latitudinal (right) strain in the balloon caused by inflation.

**Figure S2. a**, Distribution of strain across the purple dotted area in Fig. 1c, at various positions across the device thickness direction: the top PI surface, the middle of the 1<sup>st</sup> metal layer and the bottom of the bottom PI. **b**, Magnified view of strain distributions in the middle layer of temperature and tactile sensors (with epoxy), including the circumferential bridges.

**Figure S3. a**, SEM images before (left) and after (right) uniaxial stretching to 45%, showing the conversion of serpentine interconnects from their initial coplanar state (left) to non-coplanar configurations (right). **b**, Tilted view of Fig. S3a.

**Figure S4. a**, Fabrication of a stretchable electrode array on a handle wafer, illustrated with a schematic cartoon (left) and a corresponding image (right). **b**, Shadow masking for selective SiO<sub>2</sub> deposition to the backside of the island regions. **c**, Transfer printed sensor array on a thin (~300 μm), low modulus (~200 kPa) substrate of PDMS. The island regions are attached to UVO activated PDMS through strong covalent bonding, while the interconnects are weakly attached to PDMS with Van der Waals force.

**Figure S5.** **a**, Metal connector on polyimide (Kapton) film. **b**, Connection of stretchable sensor array to the circuit board through the connector illustrated in **a**, and an ACF cable.

**Figure S6.** **a**, Calculated maximum strain in PSR layers of tactile sensors with different thickness layers of epoxy. **b**, Percentage change in resistance per 100 kPa change in pressure, and average lateral expansion strain in the PSR bridge  $\epsilon_{11}$  (Fig. 2b) as a function of PDMS thickness.

**Figure S7.** Custom micro-compression stage for evaluating the tactile sensors.

**Figure S8.** Cyclic micro-compression tests on tactile sensors, at different frequencies. **a**, 0.1 Hz. **b**, 0.5 Hz. **c**, 1 Hz. **d**, 2 Hz.

**Figure S9.** **a**, Temperature sensitivity of the measured resistance from tactile sensors. **b**, Resistance change of the temperature sensor during on and off contact with 0.5 Hz frequency. **c**, Resistance change with 1 Hz frequency. **d**, Resistance change with 2 Hz frequency.

**Figure S10.** **a**, Calibration curve for the Pt temperature sensor. **b**, Change in resistance of the temperature sensor during full inflation and deflation of balloon catheter. **c**, Calibration curve for a Pt flow sensor. **d**, Percent change in resistance of a Pt flow sensor at different flow rates. **e**, Calibration curve for a Au flow sensor.

**Figure S11.** **a**, RF ablation with multiple electrodes on a balloon catheter. **b**, IR camera image of the temperature distribution during RF ablation.

**Figure S12.** The effect of the coefficient of natural convection on the temperature distribution along **a**, radial direction and **b**, thickness direction.

**Figure S13.** **a**, Contour plot of the non-dimensional function  $\theta$ . **b**, The non-dimensional function  $\theta$  versus  $z/r_0$  at  $r=0$ . **c**, The non-dimensional function  $\theta$  versus  $r/r_0$  at  $z=0$ .

**Figure S14.** Comparison of temperature distribution from FEM with temperature-dependent electrical conductivity and analytical model with an equivalent electrical conductivity 0.970S/m along **a**, radial direction and **b**, thickness direction. **c**, Calculated

temperature distribution on the surface of a rabbit heart based on measurement by a temperature sensor (location of the temperature sensor and two adjacent ablation electrodes shown by blue and red dots, respectively).

**Figure S15.** Surgical gloves with **a**, electrodes and **b**, tactile sensors. **c**, Contact signals measured by tactile sensors on surgical gloves.

**Figure S16.** **a**, Pressure sensing circuit with controlled programmable current across the tactile pressure sensor's terminals. **b**, Data flow diagram for the pressure sensing and electrophysiological mapping. **c**, Images of the data acquisition system.

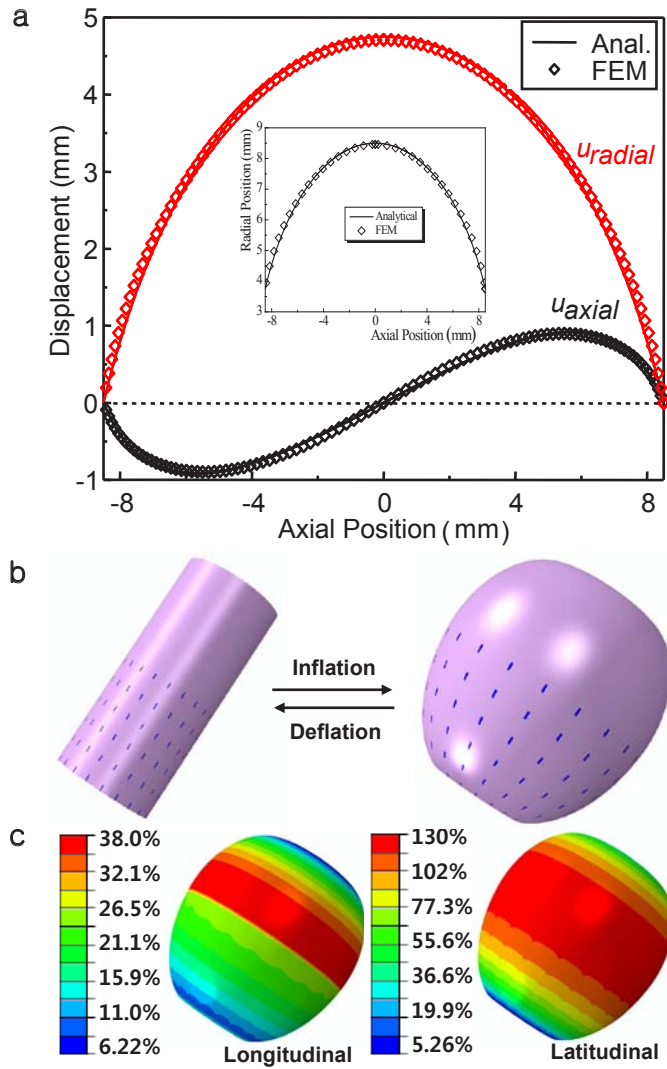


Figure S1

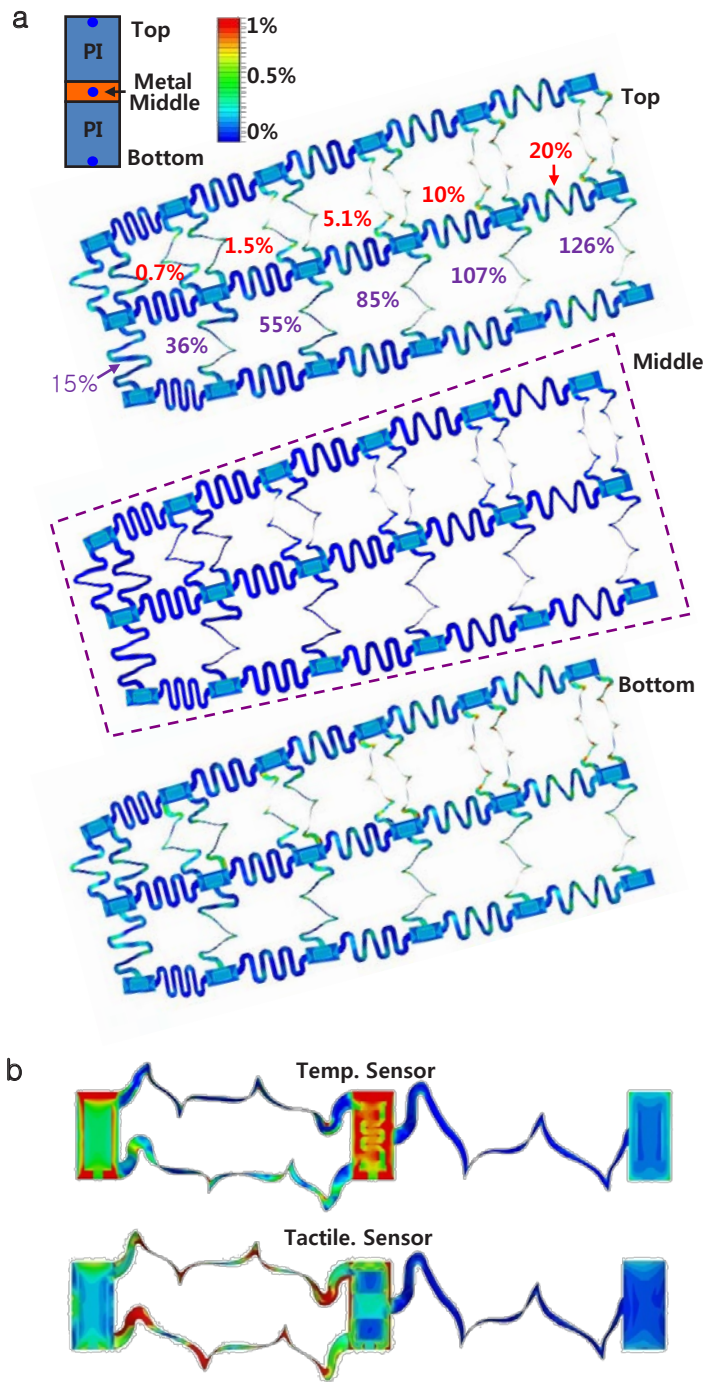


Figure S2

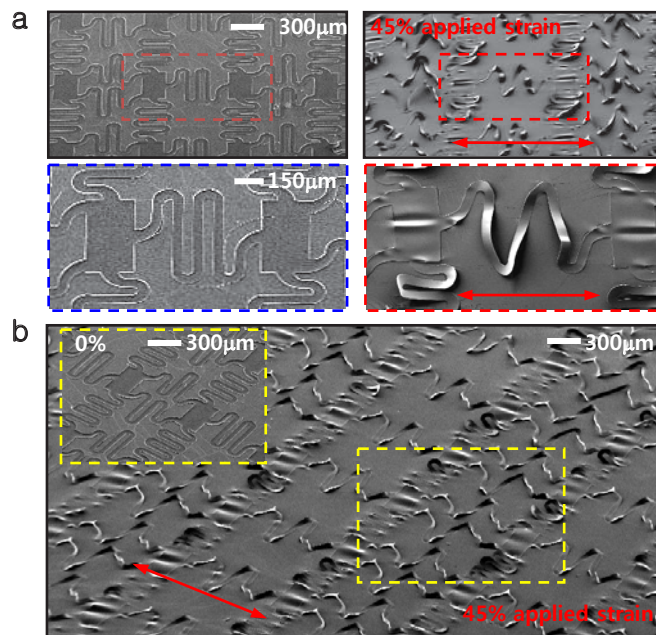


Figure S3

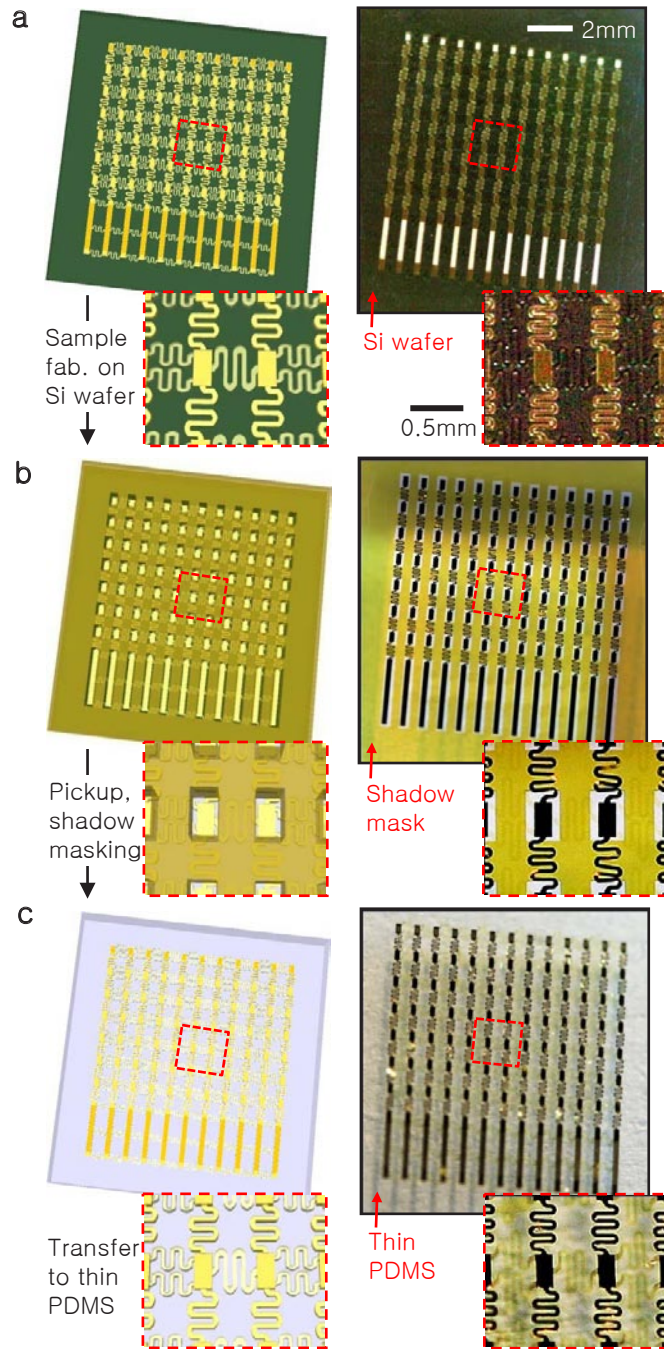


Figure S4

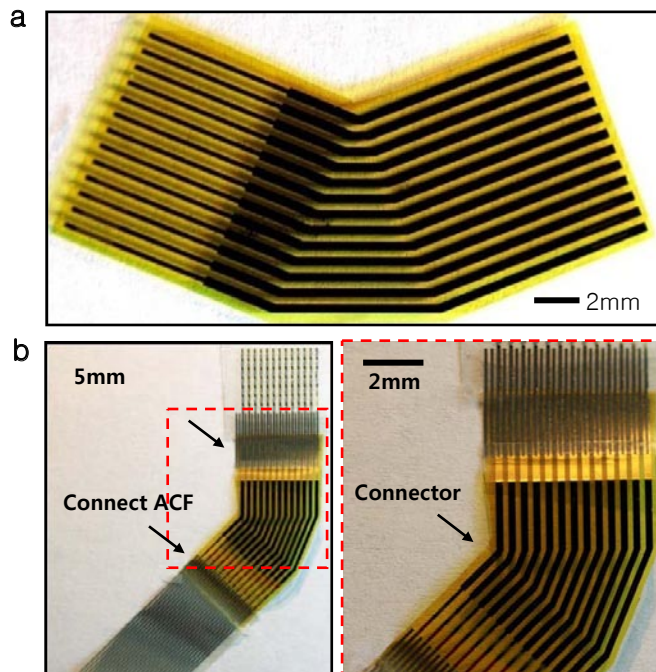


Figure S5

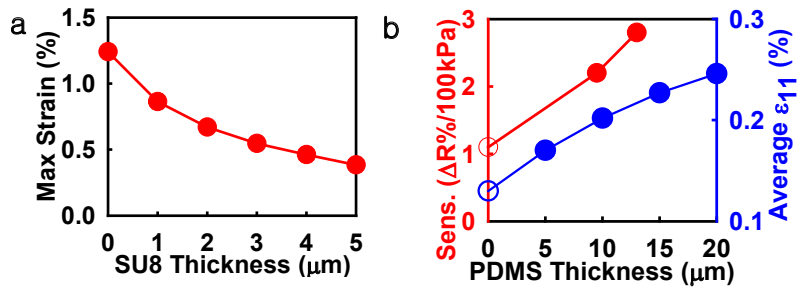


Figure S6

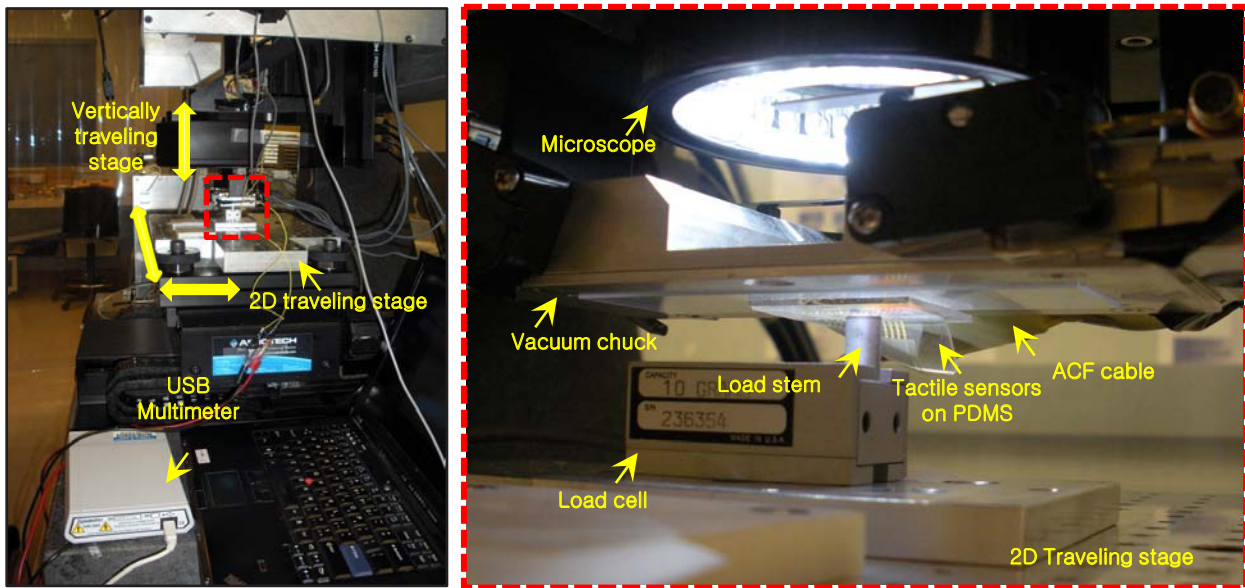


Figure S7

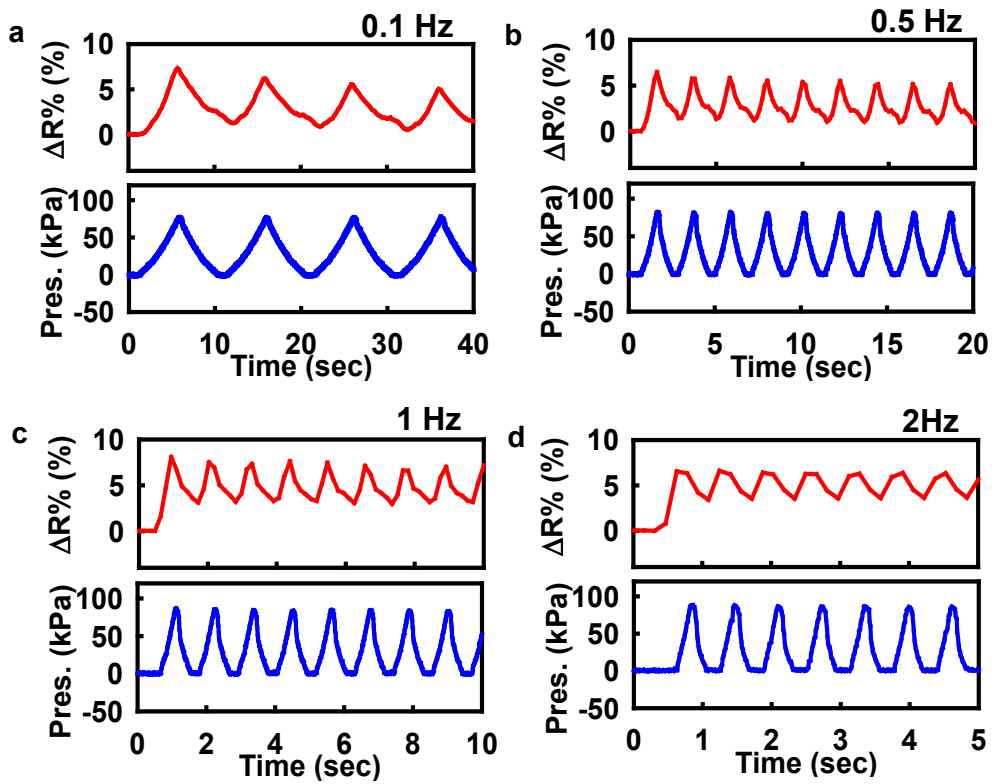


Figure S8

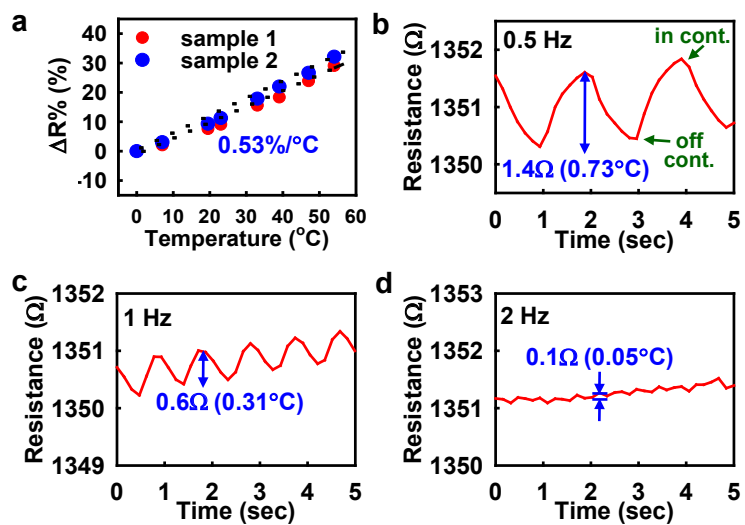


Figure S9

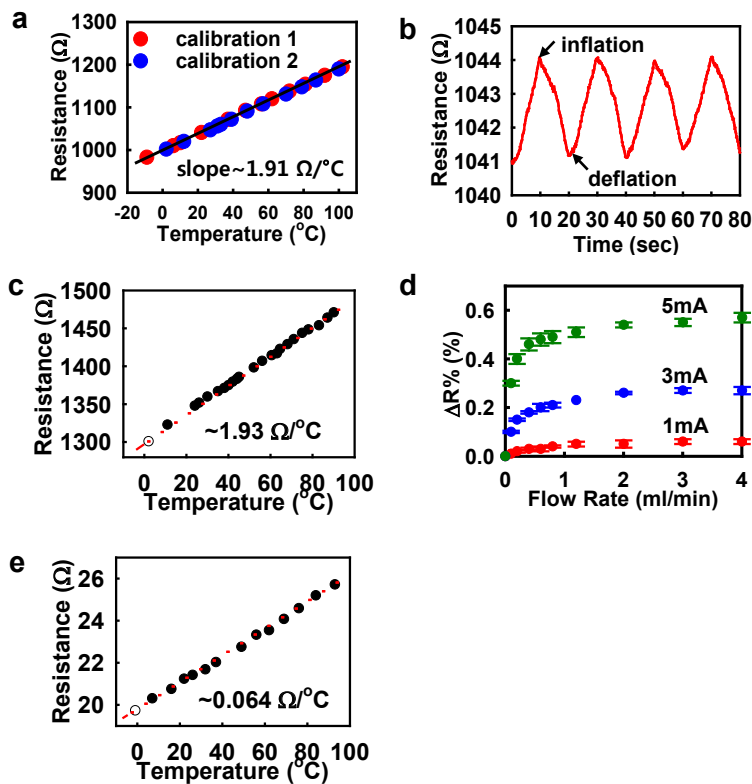


Figure S10

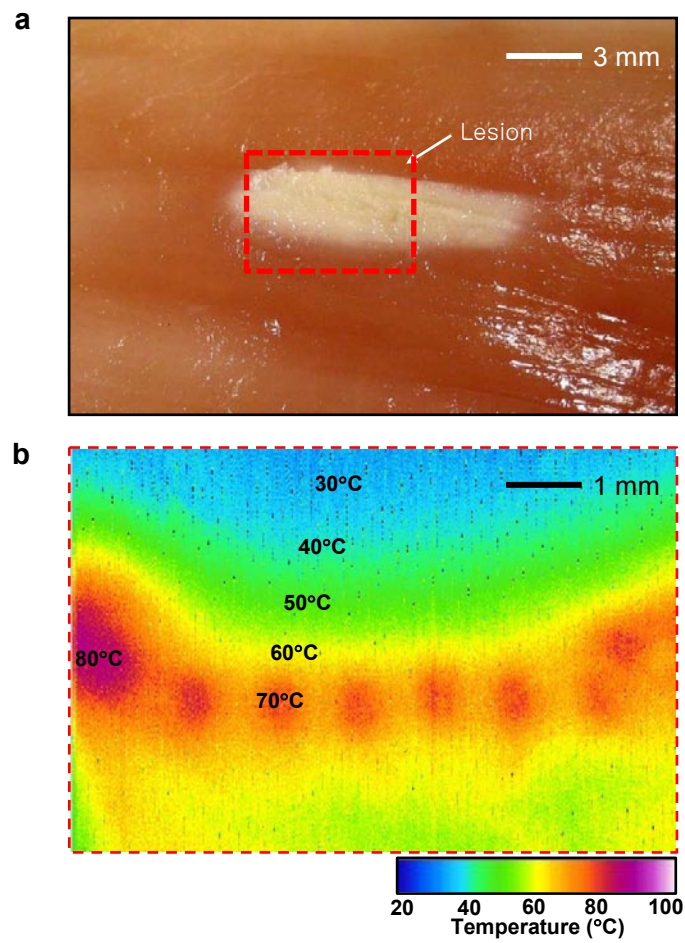


Figure S11

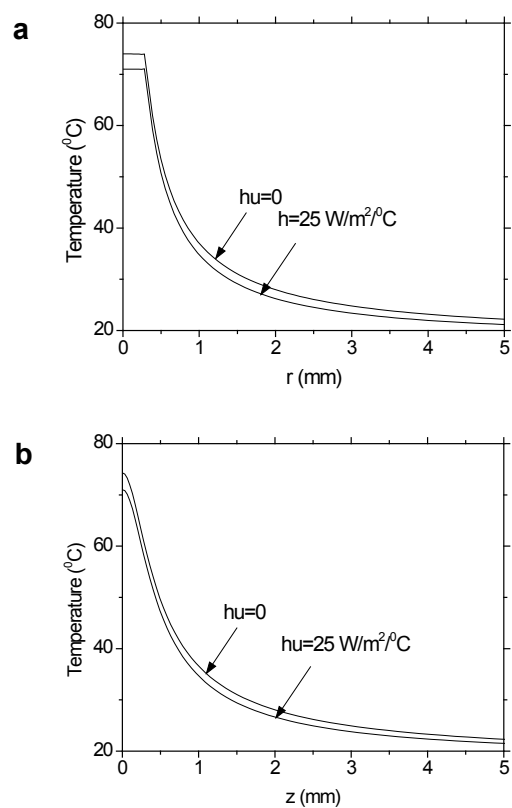


Figure S12

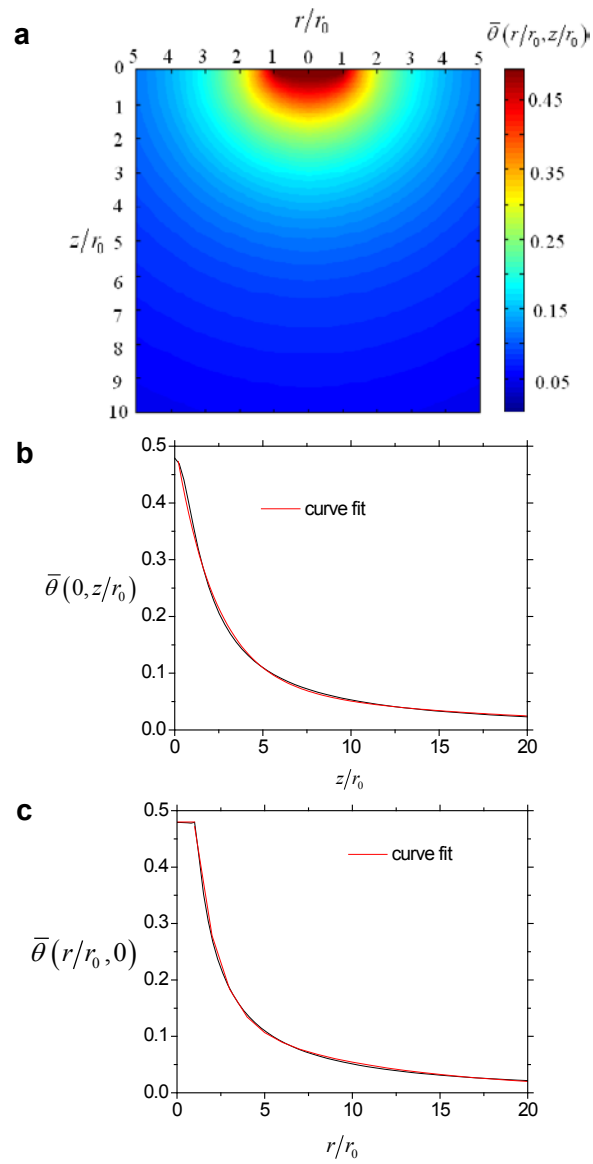


Figure S13

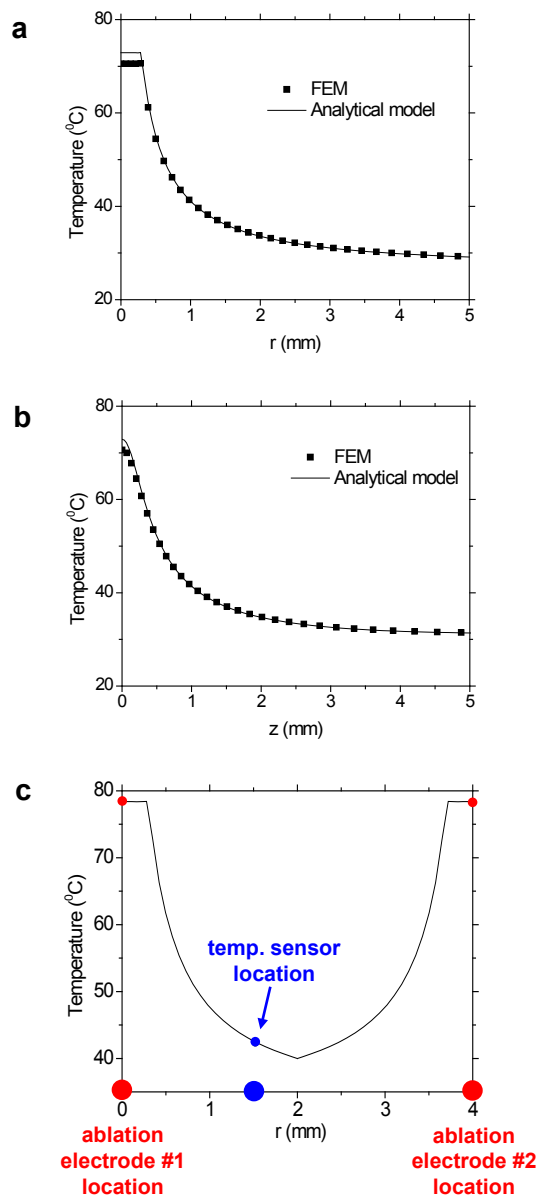


Figure S14

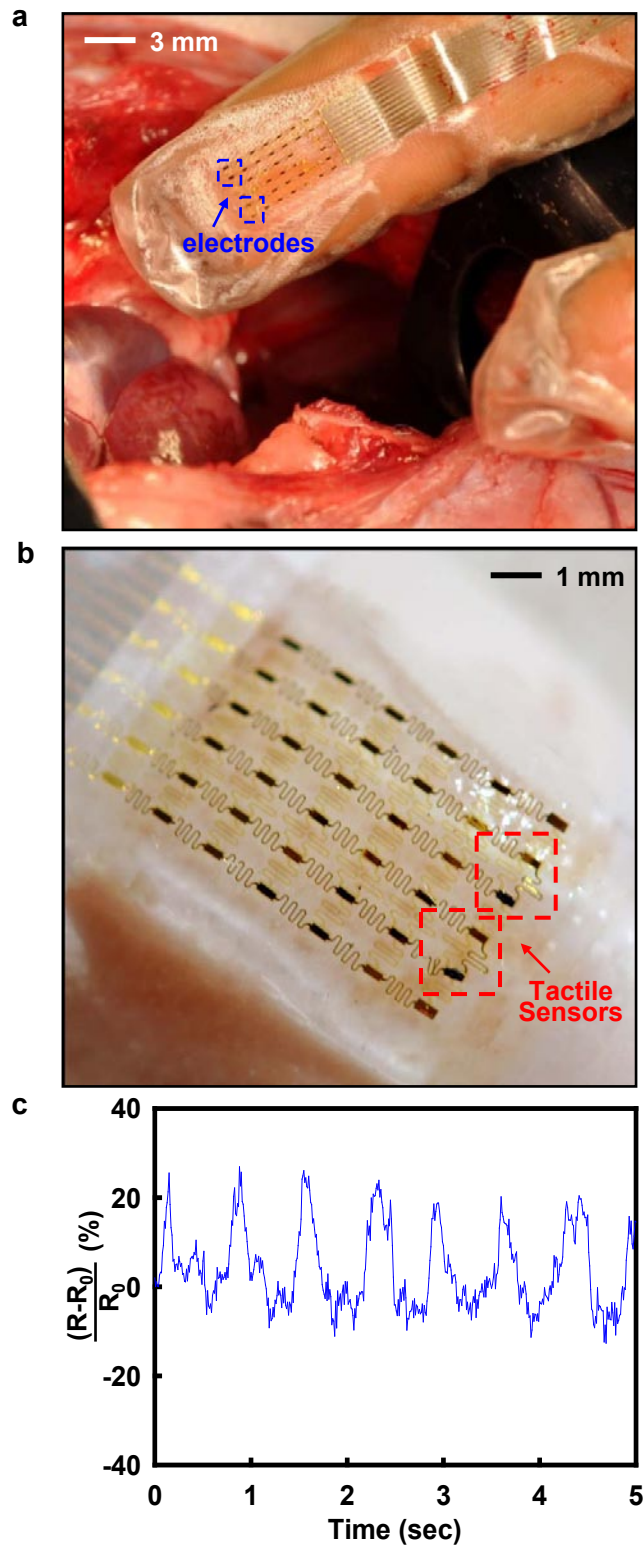


Figure S15

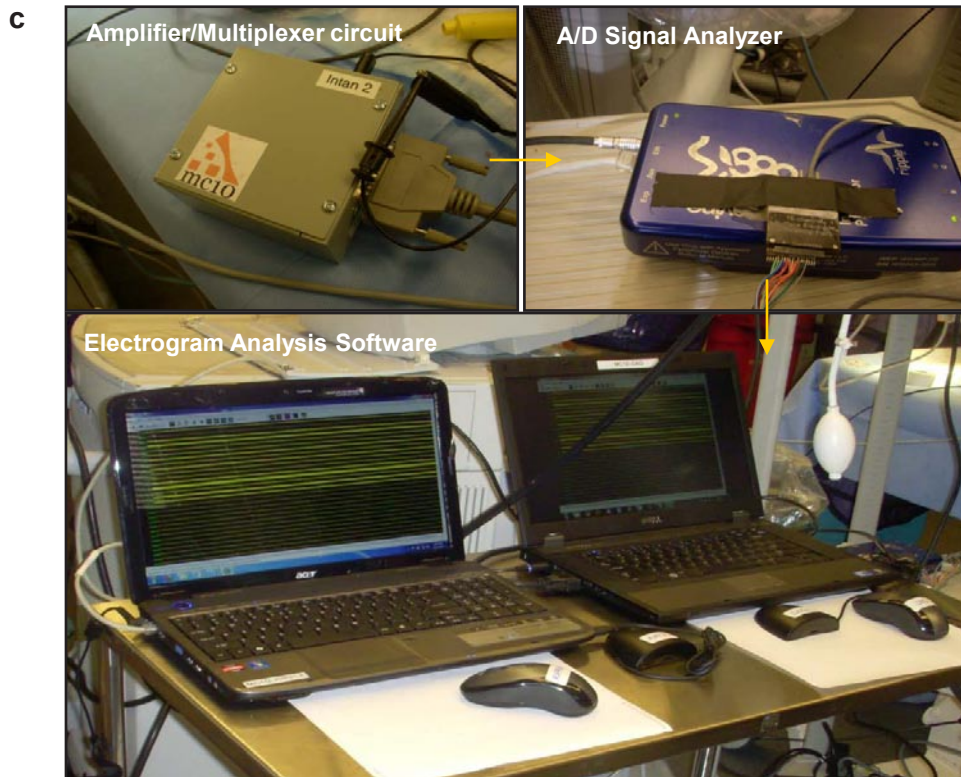
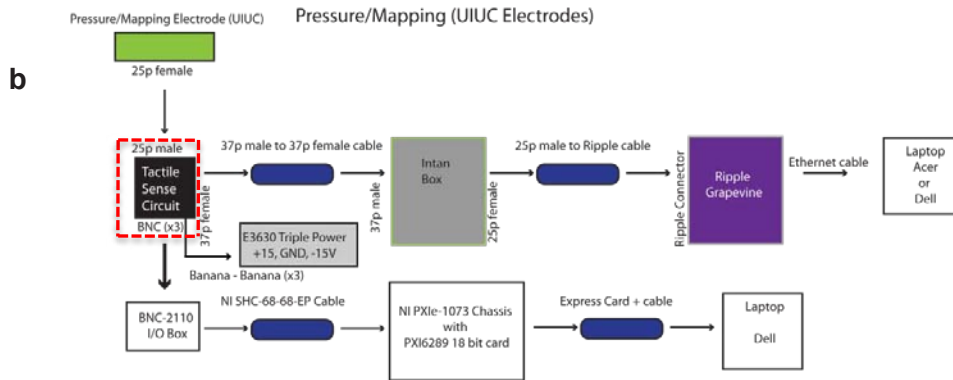
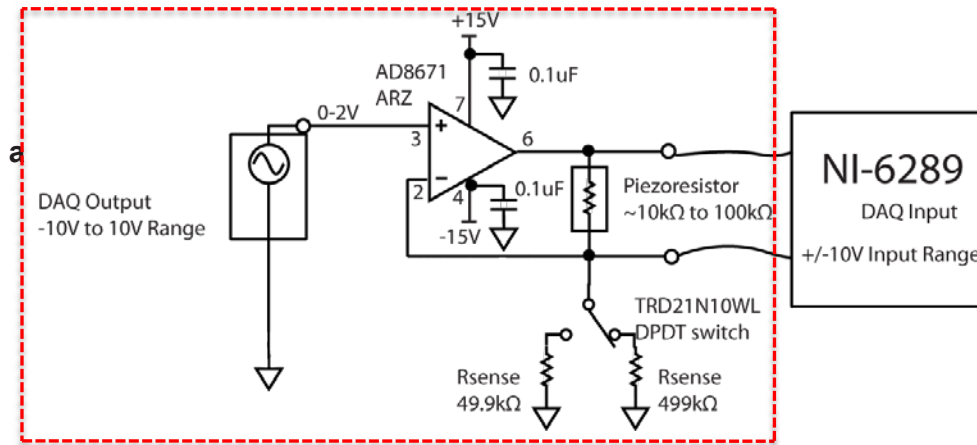


Figure S16